ADVANCED MATERIALS
www.advmat.de

Upcycling Spent Lithium-Ion Batteries: Constructing Bifunctional Catalysts Featuring Long-Range Order and Short-Range Disorder for Lithium-Oxygen Batteries

Yu Tian, Yongbin Xu, Shan Guo, Binchao Xu, Zhijun Zhao, Xinyi Yuan, Yuxiao Wang, Jianwei Li, Xiaojun Wang, Peng Wang, and Zhiming Liu**

Upcycling of high-value metals (M = Ni, Co, Mn) from spent ternary lithium-ion batteries to the field of lithium-oxygen batteries is highly appealing, yet remains a huge challenge. In particular, the alloying of the recovered M components with Pt and applied as cathode catalysts have not yet been reported. Herein, a fresh $L1_2$-type Pt_3 M medium-entropy intermetallic nanoparticle is first proposed, confined on N-doped carbon matrix ($L1_2$-$Pt_3(Ni_{1/3}Co_{1/3}Mn_{1/3})$@N-C) based on spent 111 typed $LiNi_{1-x-y}Mn_xCo_yO_2$ cathode. This well-defined catalyst combines both features of long-range order $L1_2$ face-centered cubic structure and short-range disorder in M sites. The former contributes to enhancing the structural stability, and the latter further facilitates deeply activating the catalytic activity of Pt sites. Experiments and theoretical results demonstrate that the local coordination environment and electronic distribution of Pt are both fundamentally modulated via surrounding disordered Ni, Co, and Mn atoms, which greatly optimize the affinity toward oxygen-containing intermediates and facilitate the deposition/decomposition kinetics of the thin-film Li_2O_2 discharge products. Specifically, the $L1_2$-$Pt_3(Ni_{1/3}Co_{1/3}Mn_{1/3})$@N-C catalyst exhibits an ultra-low overpotential of 0.48 V and achieves 220 cycles at 400 mA g^{-1} under 1000 mAh g^{-1}. The work provides important insights for the recycling of spent lithium-ion batteries into advanced catalyst-related applications.

1. Introduction

With the explosive growth of lithium-ion batteries (LIBs) in electric vehicles and portable devices, the efficient treatment and recycling of spent LIBs especially ternary cathode LIBs have gradually remained a significant challenge. Currently, common recycling methods for spent LIBs, such as pyrometallurgy, hydrometallurgy, and direct regeneration, are primarily aimed at returning raw materials. However, considering the unique catalytic chemical properties of the high-value metals in spent batteries, recycling these metals and applying them to other applications, such as catalysts and adsorbents, in a non-closed-loop recycling model could achieve higher-value recycling in industrial fields, which is expected to be one of the most promising directions for spent battery development in the future.[1–2] Especially, the Ni, Co, and Mn metals in spent ternary LIBs exhibit considerable performance in accelerating charge transfer and lowering reaction barriers due to their unique electronic structures and surface activities.[3] It is worth noting that aprotic lithium-oxygen batteries (LOBs), which are considered one of the ultimate energy storage technologies due to their extremely high theoretical energy density (3500 Wh kg^{-1}).[4–5] However, the typical discharge product Li_2O_2 ($2Li^+ + O_2 + 2e^- \rightleftarrows Li_2O_2$) of LOBs is insoluble and insulating, which easily blocks active sites and exacerbates the passivation effect, thereby hindering the kinetics of the oxygen reduction reaction (ORR) and oxygen evolution reaction (OER). This is the fundamental cause of the excessive polarization, low round-trip efficiency, and cycle life decay in LOBs.

Therefore, the rational design of various catalysts to regulate the morphology, crystallinity, growth path, and interfacial reaction of Li_2O_2, thereby accelerating the nucleation/decomposition efficiency of Li_2O_2, is a common strategy.[6–9] Pt-based catalysts demonstrate significant regulatory effects on addressing the aforementioned issue due to their half-filled antibonding states.[10–11] Unfortunately, Pt-based catalysts face the significant challenge of high cost and insufficient catalytic activity, which severely restricts large-scale preparation. In response, alloying Pt with 3d-transition metals is expected to reduce the Pt amount and maximize the catalytic efficiency. Specially, relative to disordered Pt-M solid solution alloys with A1 phase, the structurally ordered super-lattice structures of $L1_2$ Pt_3 M alloys are more effective

Y. Tian, Y. Xu, S. Guo, B. Xu, Z. Zhao, X. Yuan, Y. Wang, J. Li, X. Wang, P. Wang, Z. Liu
College of Electromechanical Engineering
Shandong Engineering Laboratory for Preparation and Application of High-Performance Carbon-Materials
Qingdao University of Science & Technology
Qingdao 266061, P. R. China
E-mail: pengwang@qust.edu.cn; zmliu@qust.edu.cn
Z. Liu
Qingdao Industrial Energy Storage Research Institute
Qingdao Institute of Bioenergy and Bioprocess Technology
Chinese Academy of Sciences
Qingdao 266101, P. R. China

The ORCID identification number(s) for the author(s) of this article can be found under https://doi.org/10.1002/adma.202418963

DOI: 10.1002/adma.202418963

to maintain structural stability and enhance oxidation/corrosion resistance.[12–13] For instance, Guo et al. reported a Pt_3 Pb alloy for LOBs and achieved an overpotential as low as 0.69 V at the current density of 500 mA g^{-1}.[14] Mueller et al. developed a theoretical alloy phase diagram to directly predict catalytic activity, confirming that the ordered atomic arrangement of $L1_2$-type Pt_3Ni leads to a high concentration and activity at the adsorption sites.[15] However, due to the single M component, they still suffer from the limited activation of the active Pt component for solving the slow ORR/OER kinetics. In response, benefiting from multi-element alloy effects, medium/high-entropy alloys are influenced by different coordinating elements, and the strong interactions among the components significantly activate the catalytic activity of individual elements.[16] Moreover, multi-entropy components contribute to the structural lattice distortion and the cocktail effect, further enhancing the catalytic capability within alloys.[17–18] Thus, it is reasonable to expect that the induction of multiple-entropy components at the M position in Pt_3 M might be a "Pandora's box" to completely release the catalytic activity of Pt and further improve the catalyst utilization efficiency.[19] Therefore, modulating the catalytic kinetics of Pt by multiple entropy components from spent LIBs as cathode catalyst for LOBs is highly expected, yet has not been reported to date.

Herein, based on an ultra-fast Joule-heated thermal shock method, we first convert the high-value metals from the spent 111 typed $LiNi_{1-x-y}Mn_xCo_yO_2$ based LIBs into a fresh $L1_2$-type Pt_3 M medium-entropy intermetallic nanoparticles confined on N-doped carbon matrix ($L1_2$-$Pt_3(Ni_{1/3}Co_{1/3}Mn_{1/3})$@N-C) for LOBs. This well-defined catalyst combines both features of long-range ordered $L1_2$ face-centered cubic (fcc) structure with definite stoichiometric ratios and short-range disorder in M sites. Benefiting from the unique atomic arrangement, Pt atoms of $L1_2$-$Pt_3(Ni_{1/3}Co_{1/3}Mn_{1/3})$@N-C predominantly occupy the face centers of individual $L1_2$-type grains, and the Ni, Co, Mn atoms are randomly distributed at the vertex positions of each grain. This combination of long-range order and short-range disorder not only refines the geometrical coordination environment of Pt component and accelerates electron transport, but also facilitates maintaining the structure stability. Experiments and theoretical results disclose that the medium-entropy coordination boosted 5d-3d orbital interactions between Pt atoms and the recovered Ni, Co, Mn atoms contribute to optimizing the adsorption characteristic of the oxygen-containing intermediates, tuning the rate-determining steps and thus reducing both the energy barrier of ORR and OER. During ORR, the Pt component in $L1_2$-$Pt_3(Ni_{1/3}Co_{1/3}Mn_{1/3})$@N-C serves as the active center to tightly adsorb the LiO_2 intermediates and induces the nucleation of the thin-film Li_2O_2 species, which benefits its accelerated decomposition kinetics during the following OER, thus realizing bifunctional catalytic activity. Impressively, the $L1_2$-$Pt_3(Ni_{1/3}Co_{1/3}Mn_{1/3})$@N-C catalyst harvests an ultra-low overpotential of 0.48 V and achieves 220 cycles at 400 mA g^{-1} under a cut-off capacity of 1000 mAh g^{-1}, which ranks the top among the reported catalysts, demonstrating a great application in the field of LOBs.

2. Results and Discussion

2.1. Microstructure Characterization

As shown in **Figure 1a**, $L1_2$-$Pt_3(Ni_{1/3}Co_{1/3}Mn_{1/3})$@N-C catalyst is prepared by alloying the NiCoMn component recovered from the spent ternary LIBs with the Pt precursor based on a rapid Joule-heated thermal shock process. In detail, Ni, Co, and Mn mixed ion solution is first recovered from the waste 111 typed $LiNi_{1-x-y}Mn_xCo_yO_2$ cathode from electric vehicles (see Methods). Then Pt, Ni, Co, and Mn ions with molar ratio controlled as 9:1:1:1 are homogenously chelated onto the surface of the Schiff-base polymer.[20] Afterwards, the composite powders are subjected to rapid Joule heating, during which the $Pt_3(Ni_{1/3}Co_{1/3}Mn_{1/3})$ intermetallic nanoparticles are insitu confined on the N-C substrate derived from the synchronously pyrolyzed Schiff-base polymer. It is mentioned that the second-level transient Joule-heated thermal shock not only contributes to thermodynamically driving the formation of $L1_2$ ordered alloy with super-lattice structure, but also effectively prevents the Ostwald ripening and sintering-driven agglomeration that typically occur during conventional high-temperature calcination, thereby minimizing particle size and increasing the numbers of exposed active sites.[21–22] As shown in Table S1 (Supporting Information), inductively coupled plasma optical mass spectroscopy (ICP-MS) results of $L1_2$-$Pt_3(Ni_{1/3}Co_{1/3}Mn_{1/3})$@N-C indicate that the mass fractions of Pt, Ni, Co, and Mn species are 11.43 wt.%, 0.32 wt.%, 0.37 wt.%, and 0.35 wt.%, respectively, and their molar ratios exactly match the above ratios. Therefore, this synthesis strategy facilitates the remanufacturing of valuable metals derived from spent LIBs into superior catalysts for LOBs. More importantly, the long-range ordered $L1_2$ structure significantly enhances the long-term stability of the catalyst, while the short-range disordered character of the M site triggers the cocktail effect and further activates the Pt catalytic kinetics. For comparison, single metal catalyst Pt@N-C and transition metal catalyst NiCoMn@N-C are also prepared. As shown in the scanning electron microscopy (SEM) images of N-C (Figure S1a, Supporting Information) and $L1_2$-$Pt_3(Ni_{1/3}Co_{1/3}Mn_{1/3})$@N-C (Figure S1b, Supporting information), the nanosheet morphology is still well-maintained even after undergoing the powerful thermal shock and intermetallic nanoparticles loading. The X-ray diffraction (XRD) pattern of $L1_2$-$Pt_3(Ni_{1/3}Co_{1/3}Mn_{1/3})$@N-C in Figure 1b reveals that the primary diffraction peaks located at 40.2°, 46.9°, 68.5°, and 82.6° are well matched with the Pt_3Co (JCPDS: Pt_3Co # 29–0499), which correspond to the (111), (200), (220), and (311) crystal planes, respectively.[23] Notably, obvious super-lattice diffraction peaks located at 22.9°, 32.7°, 52.5°, 58.5°, and 87.0°, which belong to (100), (110), (210), (211), and (222) crystal planes, respectively, indicate that the successful synthesis of the Pt_3 M nanocrystal with an ordered super-lattice structure. Moreover, the diffraction peaks of $L1_2$-$Pt_3(Ni_{1/3}Co_{1/3}Mn_{1/3})$@N-C slightly shift compared to Pt@N-C, attributed to the introduction of Ni, Co, and Mn atoms and special ultra-fast synthesis process leading to lattice distortion.[24] In contrast, NiCoMn@N-C only exhibits carbon peaks without metallic peaks due to the low content of M and the much smaller metal particle size.

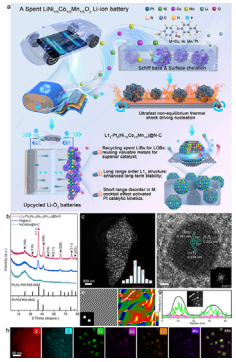

Figure 1. Synthesis, microstructure characterization of $L1_2$-$Pt_3(Ni_{1/3}Co_{1/3}Mn_{1/3})$@N-C. a) Schematic illustration of the fabrication procedures; b) XRD patterns; c) TEM image, inset showing the size distribution; d) HR-TEM image, inset showing the FFT image; e) IFFT image of (2_00) plane, and f) related strain distribution; g) line-scanning intensity distribution of Pt (green), Ni (magenta), Co (orange), and Mn (violet), respectively, insert showing the scanning nanoparticle; h) Elemental mapping images of $L1_2$-$Pt_3(Ni_{1/3}Co_{1/3}Mn_{1/3})$@N-C.

The transmission electron microscopy (TEM) image in Figure 1c displays the $L1_2$-$Pt_3(Ni_{1/3}Co_{1/3}Mn_{1/3})$ nanoparticles are uniformly and densely distributed on the whole N-C substrate with an average particle size of about 6.20 nm. Then the detailed lattice information of $L1_2$-$Pt_3(Ni_{1/3}Co_{1/3}Mn_{1/3})$@N-C is posted by high-resolution TEM (HR-TEM) as shown in Figure 1d, and the insert image shows the related fast Fourier transform (FFT) pattern. The lattice fringe spacings of 0.191 nm, 0.223 nm, and 0.224 nm are assigned to the (2_00), (1_11_), and (111_) planes of $L1_2$-$Pt_3(Ni_{1/3}Co_{1/3}Mn_{1/3})$@N-C along the [011] zone axis, respectively. Figure 1e further exhibits the inverse FFT (IFFT) pattern of the (2_00) plane, and multiple lattice distortion can be detected. The relative Geometric Phase Analysis (GPA) image of the (2_00) plane also provides more visual evidence as shown in Figure 1f. It can be seen abundant compressive and stretched strain distributed in the (2_00) plane. Similarly, as shown in Figure S2 (Supporting Information), a large strain distribution also exists at the (1_11_) and (111_) planes. In general, another $L1_2$-$Pt_3(Ni_{1/3}Co_{1/3}Mn_{1/3})$@N-C alloy nanoparticle also exhibits distinct lattice strain (Figure S3, Supporting Information). It is mentioned that the appearance of large amounts of lattice strain is usually accompanied by changes in the electronic structure, which further optimizes the intermediate adsorption characteristics.[25–26] In sharp contrast, no significant lattice distortion is observed in Pt@N-C (Figure S4, Supporting Information) and NiCoMn@N-C (Figure S5, Supporting Information). Therefore, the injection of M atoms introduces numerous lattice distortions relative to the single Pt metal, which thoroughly improves the coordination environment and electronic structure of Pt, and offers the possibility of accelerating the redox kinetics and lowering the reaction energy barriers of ORR/OER for the $L1_2$-$Pt_3(Ni_{1/3}Co_{1/3}Mn_{1/3})$@N-C catalyst. Moreover, the line-scanning across $L1_2$-$Pt_3(Ni_{1/3}Co_{1/3}Mn_{1/3})$ nanoparticles (Figure 1g) and the elemental mapping images (Figure 1h) confirm the uniform distribution of C, N, Pt, Ni, Co, and Mn.

To further monitor the detailed chemical structure and coordination environment of the $L1_2$-$Pt_3(Ni_{1/3}Co_{1/3}Mn_{1/3})$@N-C, aberration-corrected high-angle annular dark-field scanning transmission electron microscopy (HAADF-STEM) is conducted. The HAADF-STEM image of $L1_2$-$Pt_3(Ni_{1/3}Co_{1/3}Mn_{1/3})$@N-C shown in Figure S6 (Supporting Information) again verifies the uniformity of the alloy nanoparticles with an average particle size of 6.27 nm, consistent with the TEM results. The HAADF-STEM image of $L1_2$-$Pt_3(Ni_{1/3}Co_{1/3}Mn_{1/3})$@N-C in **Figure 2a** shows an intact alloy nanoparticle with clear boundaries, and the FFT image inset exhibits the (100) and (110) super-lattice electron diffraction spots (as marked by green circles), which coincides with the XRD results, further demonstrating the formation of long-range ordered structure.[27] More importantly, due to the Z-contrast, the local enlarged high magnification HAADF-STEM image shown in Figure 2b can be clearly observed that the brighter Pt atoms and the darker M atoms exhibit the periodic alternative arrangement of atomic column along the [001] zone axis. Specifically, the arrangement of atoms as the colorful balls schematic in Figure 2b is recognized to be the $L1_2$ Pt_3M-type ordered structure.[28–29] The locally enlarged false-color image originating from atomic column along the [001] zone axis (Figure 2b) shown in Figure 2c (the original uncolored image is shown in Figure S7a, Supporting Information) can more visually verify the ordered atom arrangements. Meanwhile, we perform HAADF-STEM image simulations by a multi-slice method as shown in Figure 2d and Figure S7b (Supporting Information), and the spots with alternating light-dark distribution are consistent with the previously demonstrated alternating Pt-Pt and Pt-M arrangement along the [001] zone axis.[30] Furthermore, the distribution of atomic column intensity profiles along the four atomic layers marked by dark green (L1), light green (L2), pink (L3) and blue (L4) boxes in Figure 2c are demonstrated in Figure 2e and Figure 2f. It shows a staggered distribution with a large intensity difference in L1, whereas the comparable intensity of the individual columns in L2, and the longitudinal L3 and L4 show a similar pattern of atomic column intensity distribution, which further uncovers the long-range ordered structure formed by the interleaving of the Pt-Pt atomic layers with the Pt-M atomic layers.

Moreover, the atomic column information along the [011] zone axis is also accurately captured by HAADF-STEM (Figure 2g), and the corresponding FFT image (Figure 2h) confirms the existence of (110) super-lattice diffraction spots. Based on the local magnification (Figure 2i) of Figure 2g and other identified HAADF-STEM images of $L1_2$-$Pt_3(Ni_{1/3}Co_{1/3}Mn_{1/3})$@N-C acquired along the [011] zone axis (Figures S8, S9, Supporting information), we find that the atoms exhibit highly symmetric and periodic laminar arrays and overall grid-like distribution, further corroborating the long-range ordered characteristic. Subsequently, the 3D intensity distribution is plotted as shown in Figure 2j to more visually illustrate the pattern of the Pt_3M ordered arrangement of atomic columns along the [001] zone axis. Notably, due to the extremely similar Z-contrast of M, the HAADF-STEM images only can be used to clearly distinguish Pt and M but cannot identify Ni, Co, and Mn at the M sites. Therefore, the atomic-resolution energy-dispersive spectroscopy (EDS) element mappings can provide more detailed evidence for the $L1_2$-type ordered structure of complex atomic compositions. As shown in Figure 2k, Pt atoms represented by green atoms regularly

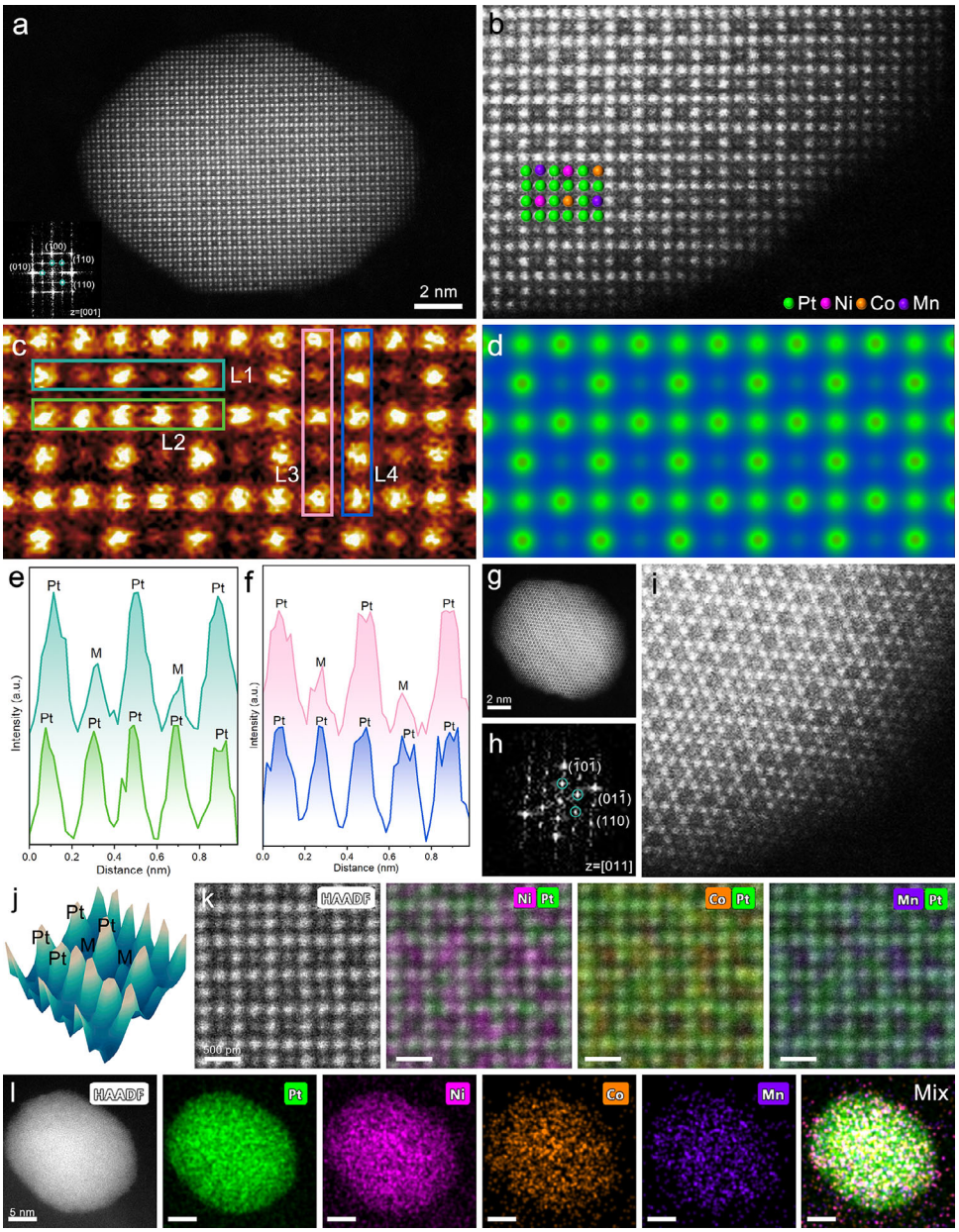

Figure 2. HAADF-STEM images of $L1_2$-$Pt_3(Ni_{1/3}Co_{1/3}Mn_{1/3})$@N-C. a) HAADF-STEM and inset of corresponding FFT pattern along the [001] zone axis of $L1_2$-$Pt_3(Ni_{1/3}Co_{1/3}Mn_{1/3})$@N-C; b) The local enlarged HAADF-STEM image from Figure 2a; c) The local enlarged false- color image along the [001] zone axis obtained from the Figure 2b; d) The simulated HAADF-STEM image along the [001] zone axis based on Figure 2c; e,f) The intensity profiles from L1, L2, L3, and L4 atomic layers marked by dark green, light green, pink, and blue lines from Figure 2c; g) HAADF-STEM and h) corresponding FFT pattern along the [011] zone axis of $L1_2$-$Pt_3(Ni_{1/3}Co_{1/3}Mn_{1/3})$@N-C; i) The local enlarged HAADF-STEM image from Figure 2g; j) The 3D intensity profiles along the [001] zone axis; k) Atomic-resolution EDS elemental mapping images of HAADF, NiPt, CoPt, and MnPt; l) EDS element mapping images of HAADF, Pt, Ni, Co, Mn and Mix.

occupy light sublattice sites, while Ni, Co, and Mn atoms represented by magenta, orange, and violet atoms, respectively, randomly occupy dark sublattice sites. In other words, Pt atoms predominantly occupy the face centers of the $L1_2$ single cell, while Ni, Co, and Mn atoms randomly occupy vertices of the $L1_2$ single cell. Similarly, EDS elemental mappings along the [011] zone axis (Figure S10, Supporting Information) are in high agreement with the above results. In this special structure, due to the significant atomic radius difference and strong electronic interactions between Pt and M atoms, Pt atoms tend to stabilize at low-symmetry positions (face-centered positions). In contrast, Ni, Co, and Mn atoms, which have similar atomic radii and weaker interactions, are randomly distributed at the vertex positions. The combination of long-range ordered Pt-Pt and Pt-M with short-range disordered M minimizes the overall structural energy, ensuring thermodynamic stability and effectively preventing phase

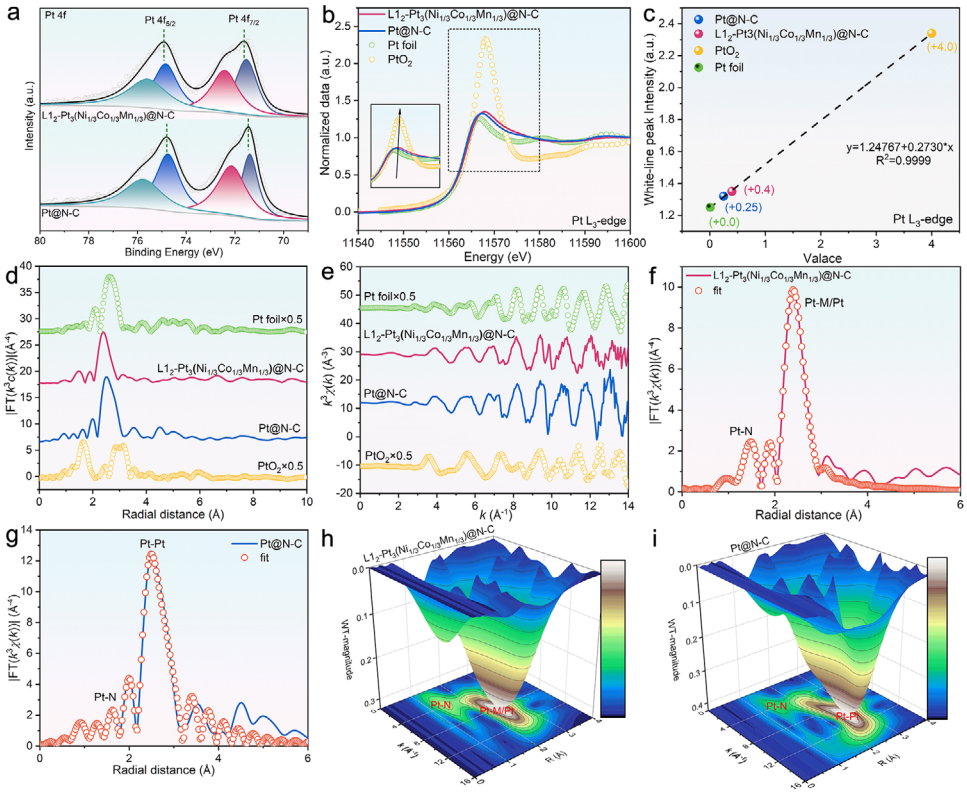

Figure 3. Structural characterizations of $L1_2$-$Pt_3(Ni_{1/3}Co_{1/3}Mn_{1/3})$@N-C and Pt@N-C. a) High-resolution XPS of Pt 4f spectra for $L1_2$-$Pt_3(Ni_{1/3}Co_{1/3}Mn_{1/3})$@N-C and Pt@N-C; b) The XANES spectra of $L1_2$-$Pt_3(Ni_{1/3}Co_{1/3}Mn_{1/3})$@N-C, Pt@N-C, Pt foil, and PtO_2, respectively; c) The fitted valence of Pt; The FT-EXAFS spectra of Pt L_3-edge for $L1_2$-$Pt_3(Ni_{1/3}Co_{1/3}Mn_{1/3})$@N-C, Pt@N-C, Pt foil, and PtO_2 in d) R space and e) k space; The corresponding FT-EXAFS fitting curves of Pt L_3-edge for f) $L1_2$-$Pt_3(Ni_{1/3}Co_{1/3}Mn_{1/3})$@N-C and g) Pt@N-C; WT-EXAFS analysis of h) $L1_2$-$Pt_3(Ni_{1/3}Co_{1/3}Mn_{1/3})$@N-C, and i) Pt@N-C.

separation or structural collapse. Moreover, the elemental mapping shown in Figure 2l and the energy dispersive X-ray (EDX) spectrum shown in Figure S11 (Supporting Information) demonstrate that the Pt, Ni, Co, and Mn elements are uniformly distributed across the whole alloy particle. Compared with the conventional alloys where each sub-lattice is basically occupied by a single type of element, the unique atomic site-occupation behavior of the $L1_2$-$Pt_3(Ni_{1/3}Co_{1/3}Mn_{1/3})$ alloy nanocrystals is mainly attributed to the rapid Joule-heated strategy. The rapid heating in an extremely short period of time contributes to the quick atoms diffusing and reaching the specific lattice positions, avoiding particle coarsening and compositional segregation brought by long-time high-temperature treatment, while the rapid quench locks the specific $L1_2$ crystal structure.[31–32] In addition, the thermodynamic driving force provided by Joule-heating enables the system to overcome the energy barrier of atomic migration and suppress the influence of surface energy on the structure.[33]

To investigate the chemical composition and electronic structure of $L1_2$-$Pt_3(Ni_{1/3}Co_{1/3}Mn_{1/3})$@N-C, Pt@N-C, and NiCoMn@N-C, X-ray photoelectron spectroscopy (XPS) and X-ray absorption spectrum (XAS) are conducted. The high-resolution N 1s spectrum (Figure S12, Supporting Information) of $L1_2$-$Pt_3(Ni_{1/3}Co_{1/3}Mn_{1/3})$@N-C suggests that N species contribute to robust metal-support interactions within $L1_2$-$Pt_3(Ni_{1/3}Co_{1/3}Mn_{1/3})$@N-C. Notably, no obvious characteristic peaks of the high-resolution Ni 2p, Co 2p, and Mn 2p spectra can be observed for $L1_2$-$Pt_3(Ni_{1/3}Co_{1/3}Mn_{1/3})$@N-C and NiCoMn@N-C due to too low M contents (Figure S13, Supporting Information). The high-resolution Pt 4f XPS spectra in **Figure 3a** exhibit that the Pt $4f_{7/2}$ (72.0 eV) and Pt $4f_{5/2}$ (75.0 eV) peaks of $L1_2$-$Pt_3(Ni_{1/3}Co_{1/3}Mn_{1/3})$@N-C shift to higher binding energy, compared to that of Pt@N-C (71.5 and 74.8 eV, respectively), indicating that Pt inclines to be electron-deficit center due to local electron repopulation caused by alloying of Pt with M. The X-ray absorption near-edge structure spectra (XANES) of Pt L_3-edge shown in Figure 3b illustrates that both the white line peak intensity and position of $L1_2$-$Pt_3(Ni_{1/3}Co_{1/3}Mn_{1/3})$@N-C and Pt@N-C are located in the middle of the standard samples Pt foil and PtO_2, which meaning that Pt atoms in $L1_2$-$Pt_3(Ni_{1/3}Co_{1/3}Mn_{1/3})$@N-C and Pt@N-C are between metallic and oxidized states. Notably, the intensity of the white line peak is related to the transition of electrons from the 2p to the 5d orbitals. Herein the higher white line peak intensity in Pt L_3-edge of $L1_2$-$Pt_3(Ni_{1/3}Co_{1/3}Mn_{1/3})$@N-C compared to Pt@N-C demonstrates that electrons are inclined to transfer from Pt atoms to adjacent M atoms, making Pt atoms be unoccupied state of 5d orbital.[34–35] Furthermore, as shown in Figure 3c, the quantitative valence state of the Pt in $L1_2$-$Pt_3(Ni_{1/3}Co_{1/3}Mn_{1/3})$@N-C is calculated by fitting calculation to be about + 0.4, which is

higher than that of Pt@N-C (+ 0.25) and faultlessly accordant with the XPS results.

To further analyze the structural evolution in more detail, the coordination environment of $L1_2$-$Pt_3(Ni_{1/3}Co_{1/3}Mn_{1/3})$@N-C, Pt@N-C, Pt foil, and PtO_2 have been fitted. As shown in the Fourier-transformed k^3-weighted extended X-ray absorption fine structures (FT-EXAFS) in R space (Figure 3d), the obvious scattering peak at 2.39 Å (nonphase-corrected) from the joint contribution of Pt-Ni/Co/Mn and Pt-Pt can be observed for $L1_2$-$Pt_3(Ni_{1/3}Co_{1/3}Mn_{1/3})$@N-C, which is smaller than Pt-Pt bond in Pt@N-C (2.52 Å) and Pt foil (2.61 Å). This is assigned to the successful coordination between Pt and M with smaller atomic radius in $L1_2$-$Pt_3(Ni_{1/3}Co_{1/3}Mn_{1/3})$@N-C. Besides, the Pt-N shell can also be observed both in $L1_2$-$Pt_3(Ni_{1/3}Co_{1/3}Mn_{1/3})$@N-C and Pt@N-C, implying strong metal-support interaction. Then, the EXAFS spectra of $L1_2$-$Pt_3(Ni_{1/3}Co_{1/3}Mn_{1/3})$@N-C and Pt@N-C are fitted in k space (Figure 3e; Figure S14, Supporting Information) and R space (Figure 3f,g). The quantitative bonding parameters are shown in Table S2 (Supporting Information). Impressively, the fitting results also prove that the bonding distance of Pt-Ni/Co/Mn shell (2.651 Å) in $L1_2$-$Pt_3(Ni_{1/3}Co_{1/3}Mn_{1/3})$@N-C is smaller than Pt-Pt coordination (2.702 Å) in Pt@N-C and Pt foil (2.761 Å). But the Pt-Pt bond length (2.782 Å) is distinctly stretched, which further suggests that lattice strain occurs in the $L1_2$-$Pt_3(Ni_{1/3}Co_{1/3}Mn_{1/3})$@N-C after alloying Pt with Ni, Co, and Mn atoms. Besides, the given coordination numbers of Pt-Pt (2.4) and Pt-Ni/Co/Mn (2.8) reveal that the active Pt atoms in $L1_2$-$Pt_3(Ni_{1/3}Co_{1/3}Mn_{1/3})$@N-C are in unsaturated coordination, which contributes to promoting the deposition/decomposition of Li_2O_2 due to the high surface energy and activity, and the unsaturated Pt atoms provide a stronger electron transfer capability that can effectively reduce the overpotential and optimize the reaction path.[36–37] The wavelet transform images of EXAFS shown in Figure 3h ($L1_2$-$Pt_3(Ni_{1/3}Co_{1/3}Mn_{1/3})$@N-C) and Figure 3i (Pt@N-C) further confirm the formation of Pt-M/Pt bonds in $L1_2$-$Pt_3(Ni_{1/3}Co_{1/3}Mn_{1/3})$@N-C again. These results prove that the optimized coordination atoms, bonding length, and coordination number benefit activating the intrinsic electronic structure of the Pt catalytic sites in $L1_2$-$Pt_3(Ni_{1/3}Co_{1/3}Mn_{1/3})$@N-C. Besides, according to the Brunauer-Emmett-Teller (BET) analysis (Figure S15, Supporting Information) and Raman spectra (Figure S16, Supporting Information) results, $L1_2$-$Pt_3(Ni_{1/3}Co_{1/3}Mn_{1/3})$@N-C exhibits a specific surface area of 369.68 $m^2\ g^{-1}$ and an I_D/I_G ratio of 0.97. The excellent specific surface area and high defectivity can provide more exposed active sites. Especially considering the specific operating processes of LOBs, these qualities of $L1_2$-$Pt_3(Ni_{1/3}Co_{1/3}Mn_{1/3})$@N-C are favorable for accommodating more discharge products and preventing active site passivation, thus enhancing the deposition/decomposition efficiency of Li_2O_2 and reducing the ORR/OER overpotential.[38]

2.2. Electrochemical Performance for LOBs

To shed light on the differences in the catalytic activity, the prepared $L1_2$-$Pt_3(Ni_{1/3}Co_{1/3}Mn_{1/3})$@N-C, Pt@N-C, and NiCoMn@N-C serve as cathode catalysts in aprotic LOBs, respectively. **Figure** 4a exhibits the cyclic voltammetry (CV) curves with a scanning speed of 0.1 mV s^{-1} at a voltage window of 2.0-4.5 V. Much higher ORR/OER peak current and enlarged cathodic/anodic integration area are obtained for the $L1_2$-$Pt_3(Ni_{1/3}Co_{1/3}Mn_{1/3})$@N-C electrode compared with Pt@N-C and NiCoMn@N-C, implying its competitive advantages in Li_2O_2 deposition/decomposition reversibility and reaction kinetics. In particular, a larger integration area also implies that more Li_2O_2 species are involved in the redox reaction, and thus the $L1_2$-$Pt_3(Ni_{1/3}Co_{1/3}Mn_{1/3})$@N-C catalysts will exhibit a higher discharge/charge capacity. Moreover, a distinct peak appears at ~2.50 V during the cathodic scan, which is primarily attributed to the reduction of O_2 to evolve into Li_2O_2. Pt@N-C and NiCoMn@N-C catalysts also basically show reduction peaks around this potential, which determines them to have similar discharge platforms. Then, during the anodic scan, the significant decomposition of surface-deposited Li_2O_2 first occurs at ≈3.17 V, and further decomposition of the thicker Li_2O_2 layer takes place at ≈3.38 V as the potential increases.[39–40] Given the unique crystal structure of long-range ordered Pt and short-range disordered M, $L1_2$-$Pt_3(Ni_{1/3}Co_{1/3}Mn_{1/3})$@N-C maximally exposes active sites, leading to significantly higher deposition/decomposition efficiency and reversibility of Li_2O_2 compared to Pt@N-C and NiCoMn@N-C. To further investigate the electrochemical performance of $L1_2$-$Pt_3(Ni_{1/3}Co_{1/3}Mn_{1/3})$@N-C electrodes in LOBs, the overpotential and round-trip efficiency of capacity-limiting ORR/OER process are measured as shown in Figure 4b and Figure S17 (Supporting Information). The $L1_2$-$Pt_3(Ni_{1/3}Co_{1/3}Mn_{1/3})$@N-C electrode exhibits the lower polarization with the overpotential of only 0.48 V (corresponding to round-trip efficiency of 78.79%) at a current density of 200 mA g^{-1} under a fixed capacity of 1000 mAh g^{-1}, while that of 0.97 V for Pt@N-C (corresponding to round-trip efficiency of 71.43%) and 1.71 V for NiCoMn@N-C (corresponding to round-trip efficiency of 57.78%). Additionally, the deep discharge/charge tests at 200 mA g^{-1} within a voltage of 2.0-4.5 V are conducted for three different electrodes. As shown in Figure 4c and Figure S18 (Supporting Information), the $L1_2$-$Pt_3(Ni_{1/3}Co_{1/3}Mn_{1/3})$@N-C cathode exhibits an ultrahigh discharge/charge capacity of 16 978.6/16 963.3 mAh g^{-1} and much lower voltage gap of 0.54 V, which is superior to those of Pt@N-C (5609.2/5551.2 mAh g^{-1}, 1.25 V) and NiCoMn@N-C (5557.9/5253.7 mAh g^{-1}, 1.86 V). Despite similar discharge plateaus at around 2.65 V during ORR, the OER catalytic process reveals significant differences due to the well-designed coordination environment and electronic structure of the Pt active centers of $L1_2$-$Pt_3(Ni_{1/3}Co_{1/3}Mn_{1/3})$@N-C. This leads to a much lower charging plateau, reducing the polarization voltage gap, and conducting in a considerably long capacity interval with a corresponding coulombic efficiency of almost close to 100% for $L1_2$-$Pt_3(Ni_{1/3}Co_{1/3}Mn_{1/3})$@N-C, which is far better than the Pt@N-C and NiCoMn@N-C electrodes.

Furthermore, the rate and cycling behavior with a limited capacity of 1000 mAh g^{-1} are also investigated. As shown in Figure 4d, the overpotential of $L1_2$-$Pt_3(Ni_{1/3}Co_{1/3}Mn_{1/3})$@N-C electrode increases from 0.13 to 0.76 V with the current density from 0.05 to 0.5 A g^{-1}, and when the density value falls back to 0.05 A g^{-1}, the overpotential recoveries to 0.27 V. This result is still much lower than that of the Pt@N-C (0.32 V) and NiCoMn@N-C (0.90 V) catalysts, which is sufficient to demonstrate the superior catalytic dynamics of $L1_2$-$Pt_3(Ni_{1/3}Co_{1/3}Mn_{1/3})$@N-C. Additionally,

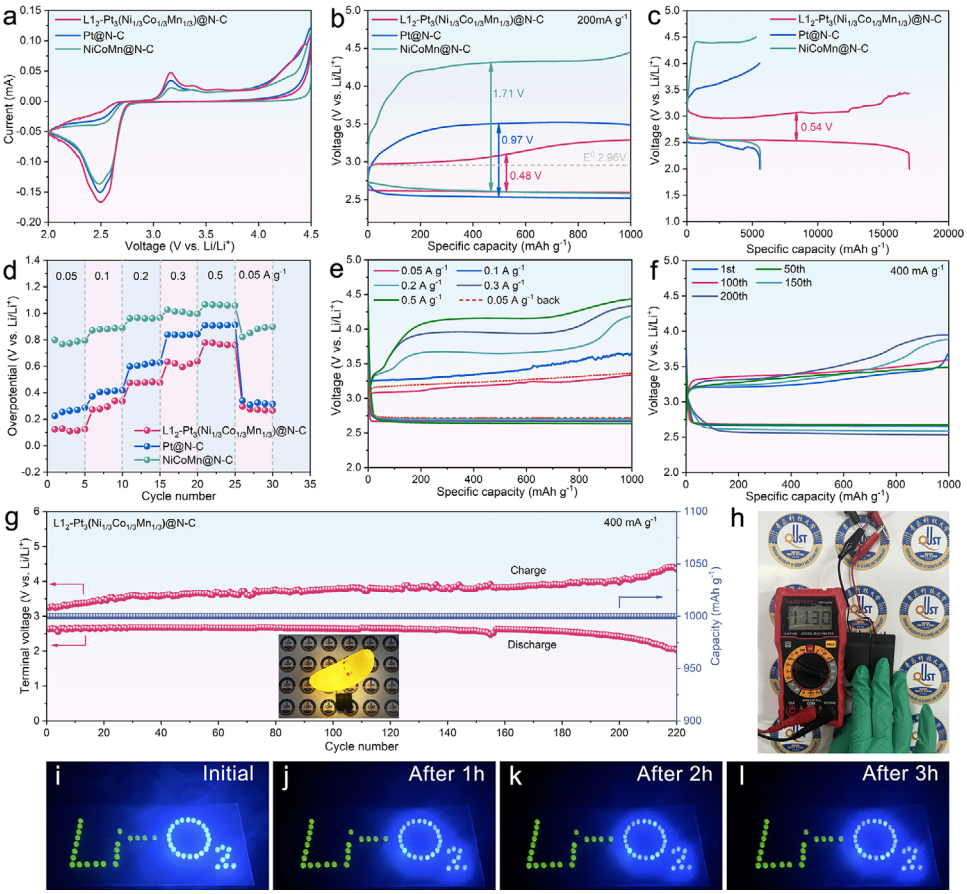

Figure 4. Electrochemical performance. a) The CV curves at 0.1 mV s^{-1} and the voltage window of 2.0-4.5 V; b) The discharge-charge curves with a fixed capacity of 1000 mAh g^{-1} at 200 mA g^{-1}; c) The deep discharge-charge curves at 200 mAg^{-1} and d) rate performance at current densities from 0.05 to 0.5 A g^{-1} with a fixed capacity of 1000 mAh g^{-1} for L1$_2$-Pt$_3$(Ni$_{1/3}$Co$_{1/3}$Mn$_{1/3}$)@N-C, Pt@N-C and NiCoMn@N-C, respectively; e) Discharge-charge profiles at current densities from 0.05 to 0.5 A g^{-1} with a fixed capacity of 1000 mAh g^{-1}; f) The discharge-charge profiles with different cycles at 400 mA g^{-1} and g) cycling performance and terminal discharge-charge voltages at 400 mA g^{-1} with a fixed capacity of 1000 mAh g^{-1} for L1$_2$-Pt$_3$(Ni$_{1/3}$Co$_{1/3}$Mn$_{1/3}$)@N-C; h) Optical photograph of four series-connected L1$_2$-Pt$_3$(Ni$_{1/3}$Co$_{1/3}$Mn$_{1/3}$)@N-C based Li-air button cells with an open-circuit voltage of 11.30 V; i–l) Optical photograph of LED powered by eight series-connected L1$_2$-Pt$_3$(Ni$_{1/3}$Co$_{1/3}$Mn$_{1/3}$)@N-C based Li-air button cells at initial, after 1 h, after 2 h and after 3 h, respectively.

Figure S19 (Supporting Information) and Figure S20 (Supporting Information) display the low discharge-charge fluctuations of terminal voltage for L1$_2$-Pt$_3$(Ni$_{1/3}$Co$_{1/3}$Mn$_{1/3}$)@N-C. The discharge/charge curves at different current densities shown in Figure 4e and Figure S21 (Supporting Information) provide more comprehensive evidence for the above results. It is proved that L1$_2$-Pt$_3$(Ni$_{1/3}$Co$_{1/3}$Mn$_{1/3}$)@N-C electrode can maintain the discharge terminal voltage around 2.65 V and stabilize the charge terminal voltage below 4.5 V at different rates. This demonstrates that during the O_2 reduction and Li_2O_2 oxidation process, the fully exposed active sites of L1$_2$-Pt$_3$(Ni$_{1/3}$Co$_{1/3}$Mn$_{1/3}$)@N-C provide abundant Li_2O_2 deposition and decomposition sites, and the long-range ordered structural framework ensures the long-term effectiveness of these active sites even at large current densities. Herein, L1$_2$-Pt$_3$(Ni$_{1/3}$Co$_{1/3}$Mn$_{1/3}$)@N-C is fundamentally optimized to ameliorate high-rate catalytic kinetics and polarization processes, promoting ORR/OER at a smaller redox voltage gap. By contrast, the charging voltage of the Pt@N-C electrode can be basically comparable to that of the L1$_2$-Pt$_3$(Ni$_{1/3}$Co$_{1/3}$Mn$_{1/3}$)@N-C electrode at the same rates, but the rapid decay of discharge voltage leads to much larger overpolarizations of the Pt@N-C electrode as the rate increases, and the reaction kinetic process of the ORR/OER is seriously hampered. What's worse, the polarization is even more serious for the NiCoMn@N-C electrode, implying its weaker catalytic effect on the deposition/decomposition of Li_2O_2.[41–42] As a result, the addition of the Pt active component bridges the gap of insufficient catalytic activity of the M components for the OER. Moreover, the catalytic activity of Pt atoms can be further stimulated by the surrounding M atoms. These two boosting effects in L1$_2$-Pt$_3$(Ni$_{1/3}$Co$_{1/3}$Mn$_{1/3}$)@N-C work together to fundamentally solve the serious polarization problem caused by the deposition/ decomposition of the insulating discharge products in LOBs. From this point, it can be inferred that the alloying of Pt with M and the coordination environment of L1$_2$-type Pt$_3$ M medium-entropy intermetallic compound plays a crucial role in accelerating both the ORR and OER catalytic kinetics. The electrochemical impedance spectroscopy (EIS) of the initial L1$_2$-Pt$_3$(Ni$_{1/3}$Co$_{1/3}$Mn$_{1/3}$)@N-C, Pt@N-C, and NiCoMn@N-C

electrodes shown in Figure S22 (Supporting Information) provide further evidence that the efficient electron transport network in $L1_2$-$Pt_3(Ni_{1/3}Co_{1/3}Mn_{1/3})$@N-C distinctly reduces the charge transfer resistance stemmed from the strong interaction between M 3d and Pt 5d orbitals. Furthermore, in order to quantify the change in impedance during charging and discharging, the EIS of $L1_2$-$Pt_3(Ni_{1/3}Co_{1/3}Mn_{1/3})$@N-C, Pt@N-C, and NiCoMn@N-C after deep discharge/recharge are also conducted, as shown in Figure S23 (Supporting Information). The results demonstrate that the $L1_2$-$Pt_3(Ni_{1/3}Co_{1/3}Mn_{1/3})$@N-C catalyst still maintains the lowest charge transfer impedance after deep discharge. It also exhibits a recovery trend that is essentially consistent with the original state after deep recharge. In contrast, the Pt@N-C and NiCoMn@N-C catalysts fail to recover due to passivation effects induced by the incomplete decomposition of discharge products.

In order to verify whether the effectiveness can be maintained of $L1_2$-$Pt_3(Ni_{1/3}Co_{1/3}Mn_{1/3})$@N-C catalyst in the long term, cycling tests with fixed cut-off capacity and current density are performed. The discharge/charge curves for $L1_2$-$Pt_3(Ni_{1/3}Co_{1/3}Mn_{1/3})$@N-C, Pt@N-C, and NiCoMn@N-C electrodes at a fixed current density of 400 mA g^{-1} and a cut-off capacity of 1000 mAh g^{-1} are revealed in Figure 4f and Figure S24 (Supporting Information). Clearly, compared to Pt@N-C and NiCoMn@N-C electrodes, the cyclic discharge/charge profiles of $L1_2$-$Pt_3(Ni_{1/3}Co_{1/3}Mn_{1/3})$@N-C electrode uncovers amazing overlap over 200 cycles. Figure 4g shows the fluctuation of the terminal voltage in the above long cycle, which demonstrates that the discharge/charge terminal voltage of $L1_2$-$Pt_3(Ni_{1/3}Co_{1/3}Mn_{1/3})$@N-C electrode can still maintain at 2.65/4.3 V with a considerably low overall overpotential even after 220 cycles. In sharp contrast, the discharge/charge terminal voltage of the NiCoMn@N-C electrode reaches 2.04/4.8 V after barely 84 cycles. It is noteworthy that the Pt@N-C electrode can maintain the discharge/charge potential at 2.65/3.5 V with low polarization for nearly 40 cycles after catalyst stabilization, but the discharging voltage reduces to 2.06 V after the 88th cycle, followed by a sudden intensification of the polarization process and complete loss of catalytic activity. Although the cycle life of Pt@N-C and NiCoMn@N-C are similar, the OER overpotential of Pt@N-C is lower evidently, indicating that the active component Pt is more dominant in promoting Li_2O_2 decomposition. Therefore, we deduce that the reason for the poor durability of the Pt@N-C electrode is that the single Pt component is basically not activated and the parasitic reaction caused by electrolyte instability cannot be effectively suppressed during cycling. Furthermore, the poor cycling performance and excessive voltage gap of NiCoMn@N-C are attributed to the weaker catalytic effects of the M components on the ORR/OER. These experimental results further identified that the unique $L1_2$ crystal structure combining the long-range regular arrangement of Pt atoms and the short-range chaotic arrangement of M atoms plays a decisive role in maintaining structural stability, especially in ensuring long-term effectiveness of Pt activity, which effectively mitigates the charging and discharging polarization and dramatically improves cycling stability. More importantly, to explore the electrochemical performance of LOBs under high catalyst loading conditions, as shown in Figure S25 (Supporting Information), the deep discharge/recharge and cycling under deep depth of discharge with a much larger loading of 4–5 mg cm^{-2} are also conducted. The results demonstrate that the $L1_2$-$Pt_3(Ni_{1/3}Co_{1/3}Mn_{1/3})$@N-C catalyst still exhibits higher discharge/charge specific capacities of 7423.4/7420.7 mAh g^{-1} and a lower polarization voltage of only 0.86 V at the current density of 200 mA g^{-1} (Figure S25a, Supporting Information). And it can still maintain 33 cycles even with a much larger cut-off capacity of 6000 mAh g^{-1} at 400 mA g^{-1}. This ensures that the $L1_2$-$Pt_3(Ni_{1/3}Co_{1/3}Mn_{1/3})$@N-C catalyst maintains excellent catalytic kinetics even under such harsh conditions, with both at high catalyst loading and high discharge of depths (DOD ≈ 80%). It is mentioned that when compared to the few reported high-DOD catalysts, this also highlights the competitive advantage of our $L1_2$-$Pt_3(Ni_{1/3}Co_{1/3}Mn_{1/3})$@N-C catalyst in improving the electrochemical performance of LOBs.[43–45] Moreover, as presented in Table S3 (Supporting Information), the performance of the $L1_2$-$Pt_3(Ni_{1/3}Co_{1/3}Mn_{1/3})$@N-C catalyst stands out compared to other recently reported alloy-based catalysts, clearly demonstrating its exceptional ability to accelerate the kinetics of LOBs. To demonstrate the practical application of $L1_2$-$Pt_3(Ni_{1/3}Co_{1/3}Mn_{1/3})$@N-C based Li-air button cells, as shown in the inset of Figure 4g and Figure S26 (Supporting Information), four $L1_2$-$Pt_3(Ni_{1/3}Co_{1/3}Mn_{1/3})$@N-C based Li-air button cells in series can light up a moon-shaped toy. As shown in Figure 4h, the open-circuit voltage of these four cells in series is measured to be up to 11.3 V. Durability is another important evaluation indicator for practical applications. Thus, we arrange and assemble 51 light-emitting diodes (LED) into a "Li-O_2" pattern, and then power them up in series with 8-button $L1_2$-$Pt_3(Ni_{1/3}Co_{1/3}Mn_{1/3})$@N-C based Li-air batteries. The whole process of the LED assembly and illumination is shown in Figure S27 (Supporting Information) and Video S1 (Supporting Information). Figure 4i shows the initial state at the time of illumination, and the brightness cannot decay after 3 h (Figure 4j-l). Therefore, these experimental results indicate the superb durability of $L1_2$-$Pt_3(Ni_{1/3}Co_{1/3}Mn_{1/3})$@N-C for practical applications in Li-air batteries.

2.3. Process Analysis During Discharge/Recharge

Ex-situ monitoring of the deposition/decomposition behavior for Li_2O_2 species is conducted to gain a deeper understanding of the fundamental factors about the rapid redox kinetics and excellent cycling stability of the $L1_2$-$Pt_3(Ni_{1/3}Co_{1/3}Mn_{1/3})$@N-C electrode. As the morphology-dictated mechanism determines the effective decomposition sites of Li_2O_2, the microstructure of Li_2O_2 deposition/decomposition after full discharge/charge is investigated using SEM.[9] As shown in **Figure 5a** and Figure S28 (Supporting Information), bent and thin-film discharge products are deposited on the surface of the $L1_2$-$Pt_3(Ni_{1/3}Co_{1/3}Mn_{1/3})$@N-C electrode after full discharge. The thin-film Li_2O_2 provides a larger contact area by uniformly distributing on the catalyst surface, which is the reason for the high discharge capacity released by $L1_2$-$Pt_3(Ni_{1/3}Co_{1/3}Mn_{1/3})$@N-C catalysts. Moreover, the strong adsorption capability of oxygen-contained intermediates and the abundant distribution of nucleation sites on the $L1_2$-$Pt_3(Ni_{1/3}Co_{1/3}Mn_{1/3})$@N-C catalyst ensure the substantial deposition of the thin-film Li_2O_2, further boosting the discharge capacity. In sharp contrast, traditional large-sized toroidal discharge products are deposited on the surfaces of the Pt@N-C electrode

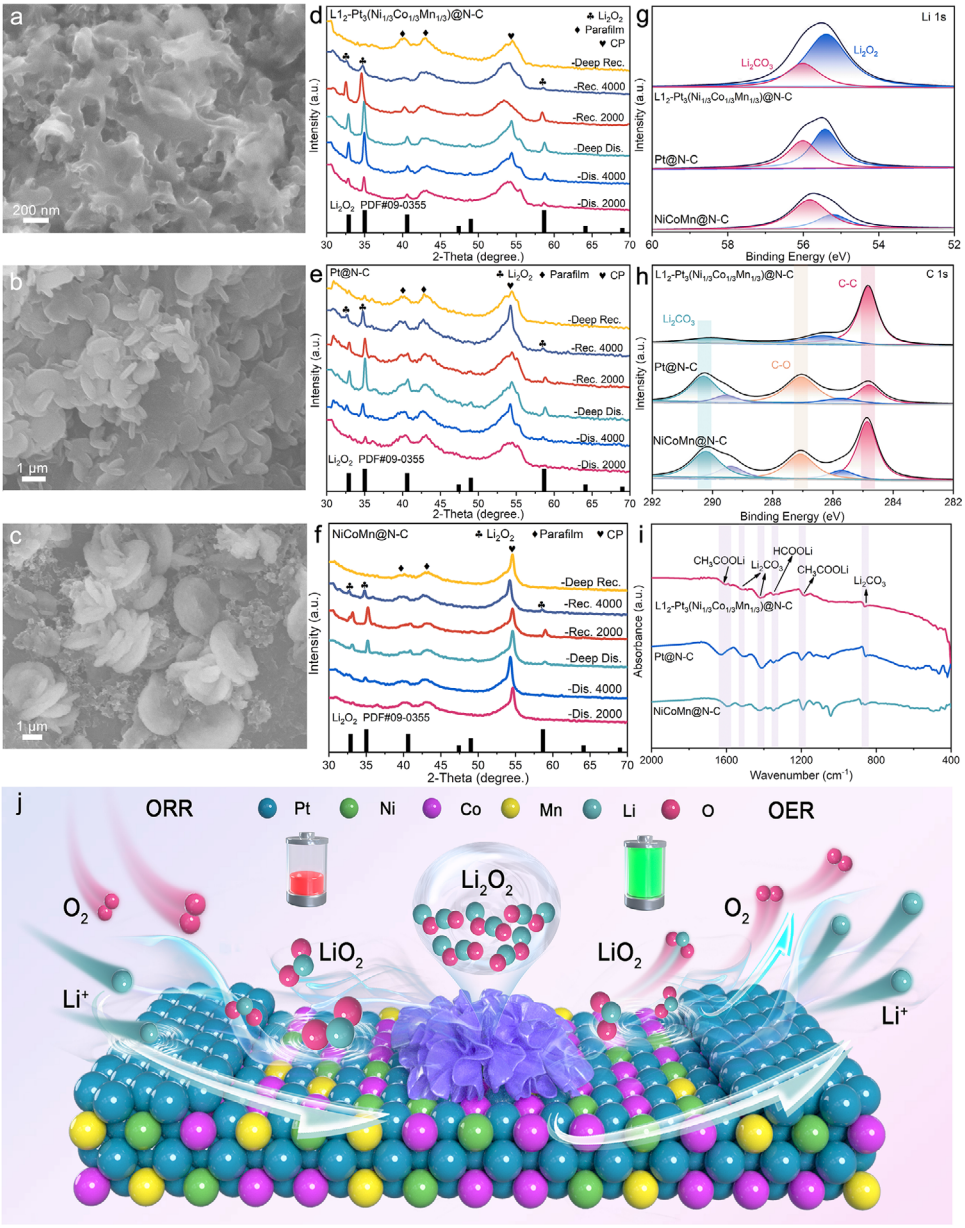

Figure 5. Process analysis during discharge/recharge Ex-situ SEM images after full discharge of a) L1$_2$-Pt$_3$(Ni$_{1/3}$Co$_{1/3}$Mn$_{1/3}$)@N-C, b) Pt@N-C and c) NiCoMn@N-C, respectively; Ex-situ XRD patterns after full discharge and full recharge of d) L1$_2$-Pt$_3$(Ni$_{1/3}$Co$_{1/3}$Mn$_{1/3}$)@N-C, e) Pt@N-C, and f) NiCoMn@N-C, respectively; Ex-situ XPS spectra of g) Li 1s and h) C 1s for L1$_2$-Pt$_3$(Ni$_{1/3}$Co$_{1/3}$Mn$_{1/3}$)@N-C, Pt@N-C, and NiCoMn@N-C after 60th cycles discharge, respectively; i) Ex-situ FTIR spectra for L1$_2$-Pt$_3$(Ni$_{1/3}$Co$_{1/3}$Mn$_{1/3}$)@N-C, Pt@N-C and NiCoMn@N-C after 60th cycles discharge, respectively; j) The reaction mechanism of L1$_2$-Pt$_3$(Ni$_{1/3}$Co$_{1/3}$Mn$_{1/3}$)@N-C.

(Figure 5b) and the NiCoMn@N-C electrode (Figure 5c). Ex-situ XRD (Figure 5d) analysis of L1$_2$-Pt$_3$(Ni$_{1/3}$Co$_{1/3}$Mn$_{1/3}$)@N-C confirms that the signal intensity of the Li_2O_2 diffraction peaks is significantly enhanced as the discharge capacity gradually increases (2000 mAh g^{-1} → 4000 mAh g^{-1} → full discharge). After full discharge, the diffraction peaks of deposits on the L1$_2$-Pt$_3$(Ni$_{1/3}$Co$_{1/3}$Mn$_{1/3}$)@N-C are measured at 32.8°, 35.0°, and 58.7°, which perfectly correspond to the (100), (101), and (110) crystal planes of Li_2O_2 (JCPDS: Li_2O_2 # 09–0355), respectively. As shown in Figure 5e,f, *ex-situ* XRD detection of the deposits on the Pt@N-C electrode and the NiCoMn@N-C electrode are also identified as Li_2O_2, with the same trend of enhanced diffraction peak signals. However, compared to the L1$_2$-Pt$_3$(Ni$_{1/3}$Co$_{1/3}$Mn$_{1/3}$)@N-C electrode, the Li_2O_2 diffraction peaks of Pt@N-C and NiCoMn@N-C electrodes exhibit much lower yield, indicating the inferior discharge capacities.

Combining the differences in the micro-morphology and structure of discharge products on different electrode surfaces during the ORR process, it can be concluded that compared with Pt@N-C and NiCoMn@N-C, the long-range ordered Pt

component and the short-range disordered M entropy component endow $L1_2$-$Pt_3(Ni_{1/3}Co_{1/3}Mn_{1/3})$@N-C with new vitality, which fundamentally alters the growth path and morphology of Li_2O_2 during the ORR process and successfully induces the nucleation of thin-film Li_2O_2.[46–47] Previous studies have shown that thin-film Li_2O_2 typically ensures smooth mass transport channels on the electrode surface due to the good conductivity, which facilitates maintaining optimal contact between Li_2O_2 and the electrode and reduces interfacial impedance.[48] Therefore, the challenge of excessively high overpotential is effectively addressed during the discharge-charge process. Additionally, the abundant exposed active sites of $L1_2$-$Pt_3(Ni_{1/3}Co_{1/3}Mn_{1/3})$@N-C can also be utilized by the thin-film Li_2O_2 with large specific surface area and uniform coverage, which is conducive to the improvement of the decomposition efficiency, and avoiding the poisoning of catalytic sites due to the excessive deposition of the Li_2O_2 layer.[49–50] In contrast, the toroidal Li_2O_2 induced by Pt@N-C and NiCoMn@N-C in contact with the electrode surface is limited, significantly restricting the transport efficiency of Li^+ and electrons.[51–52] The large volume and uneven deposition of the toroidal Li_2O_2 can lead to more severe polarization and higher overpotential. Further, the charging process has revealed the secrets of the rapid oxidation mechanism through *ex-situ* SEM and *ex-situ* XRD analysis. As shown in Figure S29 (Supporting Information), the surfaces of the $L1_2$-$Pt_3(Ni_{1/3}Co_{1/3}Mn_{1/3})$@N-C and Pt@N-C electrodes no longer show visible Li_2O_2 and reveal a smooth carbon substrate after full recharge. However, NiCoMn@N-C electrode shows suspected carbon substrate damage and accumulation of by-products even after full recharge due to the limited active sites and the high mass transfer resistance of deposited toroidal Li_2O_2.[53] Similarly, further *ex-situ* XRD validation shows that as the charging capacity increases (2000 mAh g^{-1} → 4000 mAh g^{-1} → full recharge), the Li_2O_2 peak of $L1_2$-$Pt_3(Ni_{1/3}Co_{1/3}Mn_{1/3})$@N-C (Figure 5d) is extremely weak at a recharging capacity of 4000 mAh g^{-1} and completely disappears after full recharge. This indicates that the induced thin-film Li_2O_2 with excellent conductivity and large coverage on $L1_2$-$Pt_3(Ni_{1/3}Co_{1/3}Mn_{1/3})$@N-C is efficiently decomposed during the OER process, highlighting the overwhelming advantages of the rapid redox kinetic mechanism dominated by thin-film Li_2O_2 in lowering the ORR/OER overpotential of $L1_2$-$Pt_3(Ni_{1/3}Co_{1/3}Mn_{1/3})$@N-C. However, the weak Li_2O_2 diffraction peak eventually retained in the Pt@N-C electrode (Figure 5e) implies incomplete decomposition of the discharge products. Although the complete disappearance of the Li_2O_2 characteristic peak is observed in the NiCoMn@N-C electrode (Figure 5f) due to its much lower Li_2O_2 yield, numerous by-products are detected through further chemical compositional analysis. The Li 1s and C 1s spectra of *ex-situ* XPS results (Figure 5g,h) after the 60th discharge indicate that the expected Li_2O_2 species still dominates the discharge product while the Li_2CO_3 by-product in a much lower proportion is detected for the $L1_2$-$Pt_3(Ni_{1/3}Co_{1/3}Mn_{1/3})$@N-C catalyst.[54–55] However, a significant amount of the Li_2CO_3 by-product is detected for both Pt@N-C and NiCoMn@N-C. Particularly in the case of NiCoMn@N-C, Li_2CO_3 even evolves into the dominant product, which leads to severe passivation effects and further deteriorates mass transmission pathways. To further verify the catalytic kinetics and the ability of $L1_2$-$Pt_3(Ni_{1/3}Co_{1/3}Mn_{1/3})$@N-C to suppress side reactions in LOBs, *in-situ* differential electrochemical mass spectrometry (DEMS) is conducted, as shown in Figures S30, S31 (Supporting Information). The results indicate that $L1_2$-$Pt_3(Ni_{1/3}Co_{1/3}Mn_{1/3})$@N-C exhibits significantly stronger O_2 consumption and release signals, along with extremely minimal CO_2 evolution. Further integration of the gas evolution data for $L1_2$-$Pt_3(Ni_{1/3}Co_{1/3}Mn_{1/3})$@N-C reveals that its e^-/O_2 ratio during discharge and charge is 1.91/2.04, which is remarkably close to the theoretical value of 2. As shown in Figure 5i, *ex-situ* Fourier transform infrared (FTIR) characterization results reaffirm this fact, the parasitic products embracing Li_2CO_3 (863, 1421, 1519 cm^{-1}), CH_3COOLi (1185, 1610 cm^{-1}), and HCOOLi (1349 cm^{-1}) are present in both the Pt@N-C and NiCoMn@N-C electrodes after 60th discharge. In sharp contrast, the by-product signals for the well-designed $L1_2$-$Pt_3(Ni_{1/3}Co_{1/3}Mn_{1/3})$@N-C catalyst are extremely weak.[47,52] This suggests that the long-range ordered Pt ensures structural integrity, while the activation of Pt by short-range disordered M maintains durable surface catalytic activity and promotes ORR/OER reversibility distinctly inhibiting the undesired parasitic reactions, which accounts for the key reason why $L1_2$-$Pt_3(Ni_{1/3}Co_{1/3}Mn_{1/3})$@N-C to be protected from by-products attack. In summary, the ORR/OER mechanism of $L1_2$-$Pt_3(Ni_{1/3}Co_{1/3}Mn_{1/3})$@N-C are schematically shown in Figure 5j, the nucleation of numerous thin-film Li_2O_2 is induced at the active center during ORR due to the strong constraint effect between LiO_2 and $L1_2$-$Pt_3(Ni_{1/3}Co_{1/3}Mn_{1/3})$@N-C. During the following OER, this unique Li_2O_2 accommodations with rapid decomposition advantages make full use of the regularly exposed catalytic centers, thus exhibiting much enhanced bifunctional catalytic kinetics.

2.4. Durability Analysis after Cycling

To further investigate the durability of $L1_2$-$Pt_3(Ni_{1/3}Co_{1/3}Mn_{1/3})$@N-C after cycling in LOBs, the microstructure evolutions of the catalyst after cycling are evaluated. First, the particle size and distribution homogeneity remain intact after 200 cycles by *ex-situ* TEM monitoring as shown in **Figure 6a**, illustrating that the $L1_2$-$Pt_3(Ni_{1/3}Co_{1/3}Mn_{1/3})$ nanoparticles are still firmly anchored to the N-C surface due to strong metal-support interaction, and the excellent resistance to aggregation is also well maintained in harsh electrolyte environments.[56–57] Then, as shown in Figure 6b, *ex-situ* HR-TEM results show that the lattice fringes are well defined, and the lattice spacing of 0.189 nm, 0.222 nm, and 0.224 nm is assigned to the (2_00), (1_11_), and (111_) planes of $L1_2$-$Pt_3(Ni_{1/3}Co_{1/3}Mn_{1/3})$@N-C along the [011] zone axis, respectively, which maintains a high agreement with the pattern in Figure 1d. More importantly, GPA analysis shows that the extensive lattice distortion introduced by Pt alloying with M and Joule-heated rapid thermal shock can still be accurately discerned. Figure S32 (Supporting Information) shows that the abundant stretched and compressive strains assigned to the (2_00), (1_11_), and (111_) crystal planes are well maintained and these implantation of active sites due to strain effects are exactly the key to accelerate redox kinetics, reduce overpotentials and inhibit parasitic reactions of $L1_2$-$Pt_3(Ni_{1/3}Co_{1/3}Mn_{1/3})$@N-C. The *ex-situ* TEM related evidence provided by Figure S33 (Supporting Information) again demonstrates that the exceptional

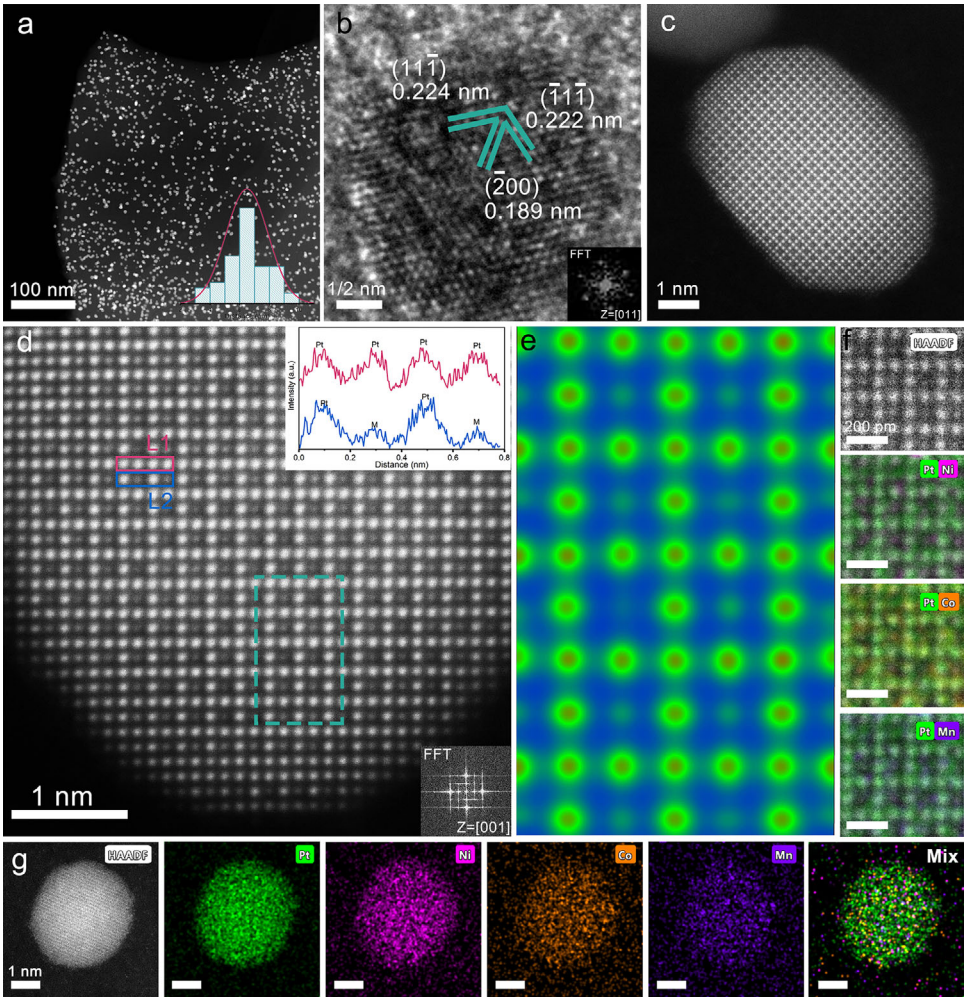

Figure 6. Ex-situ characterizations for the $L1_2$-$Pt_3(Ni_{1/3}Co_{1/3}Mn_{1/3})$@N-C catalyst after 200 cycles. a) TEM image, b) HR-TEM image, c) HAADF-STEM image, d) local enlarged HAADF-STEM image and inset of FFT image along the [001] zone axis, the intensity profiles from L1 and L2 atomic layers marked by red and blue lines, e) simulated HAADF-STEM image along the [001] zone axis based on the green dotted box of Figure 6d,f) atomic-resolution EDS elemental mapping images of HAADF, NiPt, CoPt, and MnPt and g) EDS element mapping images of HAADF, Pt, Ni, Co, Mn and Mix.

stability in terms of particle distribution, structural integrity, active site retention, and surface conditions even after 200 cycles. In addition, the *ex-situ* high magnification HAADF-STEM image (Figure 6c) provides more direct evidence that the periodic arrangement of the atoms remains intact after 200 cycles. And the locally enlarged image (Figure 6d) shows a clear distribution of atomic columns along the [001] zone axis and the arrangement is still in line with the $L1_2$-type of $L1_2$-$Pt_3(Ni_{1/3}Co_{1/3}Mn_{1/3})$@N-C. The super-lattice diffraction spots are also exceptionally obvious as shown in the embedded FFT images. Based on the results of line intensity analysis along the direction of the marked L1 and L2, the conclusion of the alternating arrangement of Pt-Pt and Pt-M is validated again. Moreover, Figure 6e illustrates a false-color image originating from the enlarged green frame of Figure 6d (the uncolored image is shown in Figure S34, Supporting Information). Alternating light and dark patches reveal a periodic arrangement of Pt occupying the face-centered locus and the M occupying vertex position, and the related visual 3D intensity distribution model is shown in Figure S35 (Supporting Information), further indicating the superior structural stability of $L1_2$-$Pt_3(Ni_{1/3}Co_{1/3}Mn_{1/3})$@N-C. Similarly, as shown in Figure S36 (Supporting Information) and Figure S37 (Supporting Information), the $L1_2$-$Pt_3(Ni_{1/3}Co_{1/3}Mn_{1/3})$@N-C catalyst after cycling remains atomically conformationally neat when observed along the [011] zone axis. Furthermore, the atomic occupation site situation is shown by the atomic-resolution EDS images (Figure 6f) and the element mapping images (Figure 6g; Figure S38, Supporting Information) also confirm the homogeneous distribution of the Pt and M atoms on specific sites, which is highly consistent with the fresh catalyst. These *ex-situ* characterizations jointly demonstrate the superior structural and compositional stability of $L1_2$-$Pt_3(Ni_{1/3}Co_{1/3}Mn_{1/3})$@N-C, which stems from the robust ordered Pt_3 M frame structure and medium-entropy stabilization effect in M site. In particular, the maintenance of the chemical state of the catalyst surface after cycling is also critical. As shown in Figure S39 (Supporting Information), the Pt 4f XPS spectrum of $L1_2$-$Pt_3(Ni_{1/3}Co_{1/3}Mn_{1/3})$@N-C after 200 cycles exhibits a slight shift toward higher binding energy. This

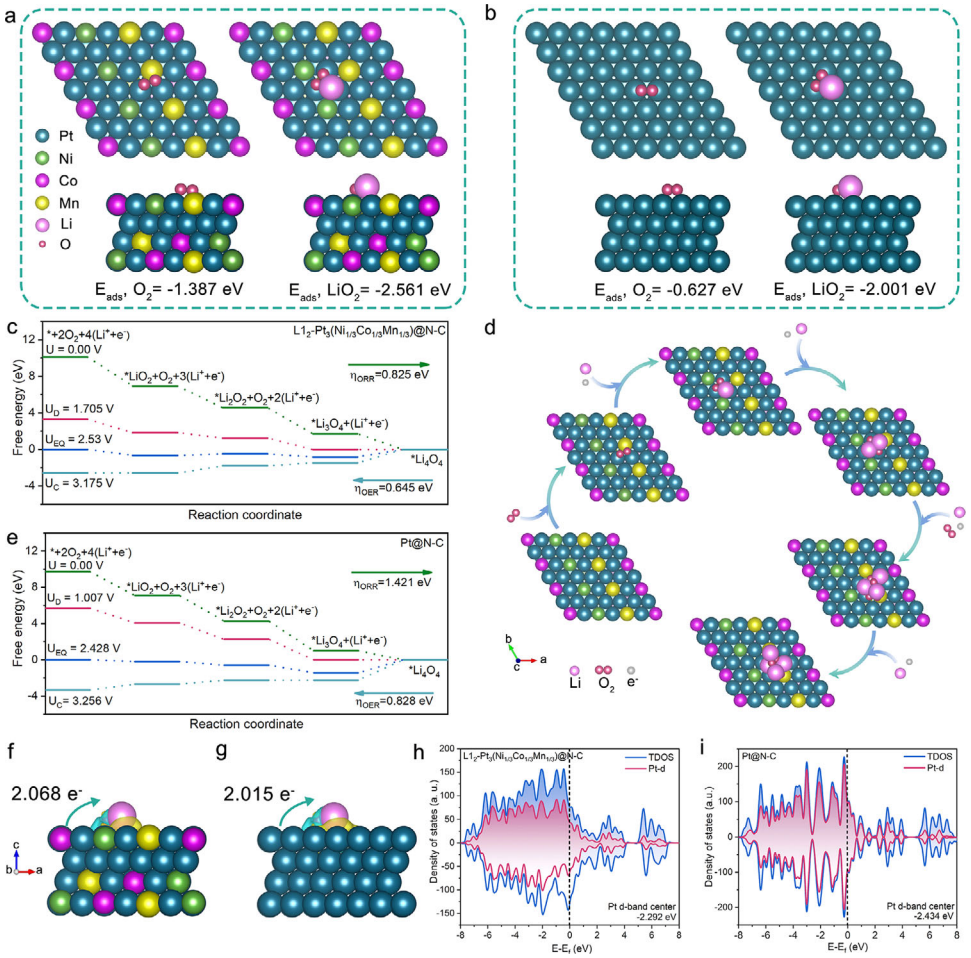

Figure 7. DFT calculations. The optimized structures of O_2 and LiO_2 adsorbed on a) $L1_2$-$Pt_3(Ni_{1/3}Co_{1/3}Mn_{1/3})$@N-C and b) Pt@N-C. c) The Gibbs free-energy step diagram for the discharge-charge reactions and d) the evolution process of Li_2O_2 of $L1_2$-$Pt_3(Ni_{1/3}Co_{1/3}Mn_{1/3})$@N-C. e) The Gibbs free-energy step diagram for the discharge-charge reactions of Pt@N-C; Charge density differences for LiO_2 adsorbate and charge transfer number of f) $L1_2$-$Pt_3(Ni_{1/3}Co_{1/3}Mn_{1/3})$@N-C and g) Pt@N-C from side view. The TDOS and DOS spectra of h) $L1_2$-$Pt_3(Ni_{1/3}Co_{1/3}Mn_{1/3})$@N-C and i) Pt@N-C.

indicates that only minor surface oxidation of Pt occurred during the catalytic process under harsh electrolyte environment, which is closely related to the incorporation of the multi-entropy components that suppress excessive oxidation or deactivation of Pt.

2.5. Density Functional Theory (DFT) Calculations

DFT simulations are conducted to further clarify the significantly enhanced catalysis kinetics of the $L1_2$-$Pt_3(Ni_{1/3}Co_{1/3}Mn_{1/3})$@N-C catalyst. Initially, as shown in Figure S40 (Supporting Information), the two active sites of Pt-containing catalysts are simulated to construct the structure models of $L1_2$-$Pt_3(Ni_{1/3}Co_{1/3}Mn_{1/3})$@N-C and Pt@N-C. Typically, the ORR is operated in LOBs first, where Li^+ reacts with O_2 adsorbed on the surface of the catalyst and an additional electron to generate the oxygen-involved intermediate LiO_2. Subsequently, LiO_2 can further react with additional electrons to form Li_2O_2 or through a self-assembly chemical disproportionation pathway evolve into Li_2O_2.[58–59] Therefore, the difference in adsorption strength of the $L1_2$-$Pt_3(Ni_{1/3}Co_{1/3}Mn_{1/3})$@N-C and Pt@N-C for O_2 and the vital intermediates LiO_2 is the key factor, and the optimized adsorption structures toward O_2 and LiO_2 are shown in Figure 7a,b and Figure S41 (Supporting information).[44] Evidently, the adsorption energies of O_2 and LiO_2 on $L1_2$-$Pt_3(Ni_{1/3}Co_{1/3}Mn_{1/3})$@N-C (-1.387 eV and -2.561 eV, respectively) are much stronger than those on Pt@N-C (-0.627 eV and -2.001 eV, respectively). It indicates that O_2 and LiO_2 will firmly immobilize on the surface of the $L1_2$-$Pt_3(Ni_{1/3}Co_{1/3}Mn_{1/3})$@N-C catalyst, which is conducive to inducing the deposition of curved and dense thin-film Li_2O_2 in the surface growth route and accelerating the kinetic reaction rate, while the weaker adsorption capacity of Pt@N-C prefers to deposit toroidal Li_2O_2 products in the path of self-assembled LiO_2. This is consistent with the actual Li_2O_2 deposition morphology of $L1_2$-$Pt_3(Ni_{1/3}Co_{1/3}Mn_{1/3})$@N-C and Pt@N-C.

Based on the above analysis of the adsorption of O_2 and LiO_2 by the $L1_2$-Pt_3 $(Ni_{1/3}Co_{1/3}Mn_{1/3})$@N-C and Pt@N-C catalysts, the integral charging and discharging mechanism is more

explicit. Therefore, the complete ORR and OER processes of the $L1_2$-$Pt_3(Ni_{1/3}Co_{1/3}Mn_{1/3})$@N-C catalyst are demonstrated by the Gibbs free energy path of nucleation/decomposition of $(Li_2O_2)_2$ clusters shown in Figure 7c. During the discharge process, the $L1_2$-$Pt_3(Ni_{1/3}Co_{1/3}Mn_{1/3})$@N-C catalyst initially adsorbs oxygen molecules and then undergoes a reduction with one Li^+ and one electron to produce the intermediate LiO_2 ($Li^+ + O_2 + e^- \rightarrow LiO_2$). Subsequently, the strong affinity of $L1_2$-$Pt_3(Ni_{1/3}Co_{1/3}Mn_{1/3})$@N-C for LiO_2 results in the inability of LiO_2 to be freely assembled to undergo the disproportionation reaction. Instead, intermediate LiO_2 continues to participate in the ORR with an additional electron and depositing it on the electrode surface to form the final discharge product Li_2O_2 according to the surface growth route ($LiO_2 + Li^+ + e^- \rightarrow Li_2O_2$). This process is shown schematically in Figure 7d and the charging process is reversed. Similarly, the Gibbs free energy path of $(Li_2O_2)_2$ clusters for Pt@N-C catalysts is shown in Figure 7e, and the specific ORR process is shown in Figure S42 (Supporting Information). In addition, the rate-determining step (RDS) and overpotential of $L1_2$-$Pt_3(Ni_{1/3}Co_{1/3}Mn_{1/3})$@N-C and Pt@N-C are also investigated through the Gibbs free energy path.[45,60] For $L1_2$-$Pt_3(Ni_{1/3}Co_{1/3}Mn_{1/3})$@N-C, the RDS of the ORR is the reduction of Li_3O_4 to Li_4O_4, while the RDS of the OER is the oxidation of LiO_2 to O_2. The RDS of Pt@N-C during ORR is the same as that of $L1_2$-$Pt_3(Ni_{1/3}Co_{1/3}Mn_{1/3})$@N-C, but the RDS for the decomposition of $(Li_2O_2)_2$ is the oxidation of Li_3O_4 to Li_2O_2. It suggests that the combination of long-range ordered Pt and short-range disordered M fundamentally affects the decomposition of Li_2O_2 as compared to single-component Pt@N-C. Furthermore, the overpotential calculations are performed to further compare the catalytic activity of the $L1_2$-$Pt_3(Ni_{1/3}Co_{1/3}Mn_{1/3})$@N-C and Pt@N-C, and the potential changes during ORR and OER are expressed as $\eta_{ORR} = U_{eq}$-U_d and $\eta_{OER} = U_c$-U_{eq}, respectively (Where U_{eq} represents the charge balance potential, U_d represents the discharge potential, and U_c represents the charge potential), while the voltage gap between U_c and U_d is defined as the total overpotential. In detail, the ORR overpotential (0.825 eV) and OER overpotential (0.645 eV) of $L1_2$-$Pt_3(Ni_{1/3}Co_{1/3}Mn_{1/3})$@N-C catalyst are both lower than those of Pt@N-C (1.421 eV and 0.828 eV, respectively). The overall overpotential of $L1_2$-$Pt_3(Ni_{1/3}Co_{1/3}Mn_{1/3})$@N-C is lower 0.779 V than Pt@N-C (Figure S43, Supporting Information). The results indicate that the coordination of short-range disordered M atoms with long-range ordered Pt atoms optimizes the local charge distribution near the active Pt centers, facilitating rapid charge transfer and overcoming high energy barriers, thereby the driving efficiency for ORR/OER can be enhanced and achieve bifunctional catalysis, which is consistent with the experimental observations shown in Figure 4b.

More importantly, the charge transfer between the catalyst and the LiO_2 in terms of charge reaction kinetics is analyzed, and the associated charge density difference distribution and Bader charge analysis are shown in Figure 7f,g, and Figure S44 (Supporting Information), respectively. Obviously, compared with Pt@N-C (2.015 e^-), the charge accumulation and depletion near the active component Pt in $L1_2$-$Pt_3(Ni_{1/3}Co_{1/3}Mn_{1/3})$@N-C are more pronounced, indicating that the surrounding charges are induced to rearrange with more electrons being transferred to LiO_2 (2.068 e^-). The enhancement of charge transfer between $L1_2$-$Pt_3(Ni_{1/3}Co_{1/3}Mn_{1/3})$@N-C and LiO_2 facilitates accelerating the nucleation/decomposition of Li_2O_2. Similarly, the electron transfer between $L1_2$-$Pt_3(Ni_{1/3}Co_{1/3}Mn_{1/3})$@N-C/Pt@N-C and O_2 (Figure S45, Supporting Information) also shows an overwhelming advantage for the former one. In order to gain deeper insight into the effect of charge rearrangement on the reaction strength between $L1_2$-$Pt_3(Ni_{1/3}Co_{1/3}Mn_{1/3})$@N-C and adsorbates, electronic densities of states (DOSs) are utilized to elucidate the detailed electronic distribution of $L1_2$-$Pt_3(Ni_{1/3}Co_{1/3}Mn_{1/3})$@N-C.[61–62] As shown in Figure 7h,i, the total electronic densities of states (TDOS) of Pt@N-C is mainly contributed by the Pt-d orbitals, whereas the alloying of Pt with M elements in the $L1_2$-$Pt_3(Ni_{1/3}Co_{1/3}Mn_{1/3})$@N-C catalyst leads to strong bonding of Pt with M, which co-shares the TDOS contribution. Notably, the d-band center of $L1_2$-$Pt_3(Ni_{1/3}Co_{1/3}Mn_{1/3})$@N-C (-2.292 eV) is positively shifted compared to that of Pt@N-C (-2.434 eV). According to the d-band center theory, the catalyst energy bands hybridize to form bonding and antibonding states when coupled with the adsorbate energy bands, as shown in Figure S46 (Supporting Information). In general, the antibonding state is commonly considered to be located near or above the Fermi energy level, while only below the Fermi energy level can be populated by electrons.[63–64] Therefore, a positive shift of the d-band center leads to a positive shift of the antibonding state produced by the coupling, which in turn reduces the filling of electrons on the antibonding state and enhances the stability of the catalyst bonding to the adsorbate.[65] This rationally elucidates the reason why $L1_2$-$Pt_3(Ni_{1/3}Co_{1/3}Mn_{1/3})$@N-C exhibits a stronger affinity for the intermediate adsorbate LiO_2 compared to Pt@N-C. Therefore, based on the experimental and computational analysis, it is concluded that short-range disordered M optimizes the local coordination environment and electronic structure of the long-range ordered active center Pt, which adjusts the d-band center position and thus promotes the adsorption capability of the oxygen-containing intermediates. This ultimately affects the nucleation-decomposition behaviors of Li_2O_2 and improves the redox kinetics and electrochemical performances of $L1_2$-$Pt_3(Ni_{1/3}Co_{1/3}Mn_{1/3})$@N-C-based LOBs.

3. Conclusion

In summary, we propose for the first time an interesting strategy for upcycling Ni, Co, and Mn valuable metals from spent LIBs into a bifunctional catalyst for LOBs by a rapid Joule-heated thermal shock method. HAADF and XAS results disclose the $L1_2$-$Pt_3(Ni_{1/3}Co_{1/3}Mn_{1/3})$@N-C catalyst with a long-range ordered Pt atoms and a short-range disordered M (M = Ni, Co, Mn) component periodically aligned according to the $L1_2$ crystal configuration. The long-range ordered Pt_3 M configuration forms a solid scaffold to ensure structural stability, while the short-range disordered M component is fundamental for activating the active component Pt by virtue of intense 5d-3d orbital interactions and medium-entropy promotion effects. This plays a key role in triggering local electronic rearrangement and thus optimizing the electronic structure of Pt catalytic sites. Experimental and simulation analysis indicates that the $L1_2$-$Pt_3(Ni_{1/3}Co_{1/3}Mn_{1/3})$@N-C catalyst with the optimized adsorption capacity of oxygen-containing intermediates and faster electron transfer efficiency demonstrates much lowered reaction energy barrier of ORR/OER. According to *ex-situ* characterizations,

the well-defined $L1_2$-$Pt_3(Ni_{1/3}Co_{1/3}Mn_{1/3})$@N-C catalyst induces the nucleation of numerous thin-film Li_2O_2 around the active sites during ORR, which demonstrates rapid decomposition kinetics during OER. As expected, $L1_2$-$Pt_3(Ni_{1/3}Co_{1/3}Mn_{1/3})$@N-C harvests much ameliorated ORR/OER bifunctional catalytic kinetics for LOBs. This work offers new perspectives for recycling spent ternary LIBs into high-efficiency medium/high-entropy alloy or intermetallic compound catalysts for metal-air batteries and beyond.

4. Experimental Section

Experiment details are provided in the ESI. †

Supporting Information

Supporting Information is available from the Wiley Online Library or from the author.

Acknowledgements

This work was funded by the National Natural Science Foundation of China (Grant Nos. 21905152, 52302273), the Taishan Scholar Project of Shandong Province of China (Grant Nos. tsqn202211160 and tsqn202312199), the Youth Innovation Team Project for Talent Introduction and Cultivation in Universities of Shandong Province, the Shandong Provincial Natural Science Foundation of China (Grant Nos. ZR2023QE176), Science and Technology Special Project of Qingdao City (24-1-8-cspz-12-nsh), and the China Postdoctoral Science Foundation (Grant Nos. 2022M713249).

Conflict of Interest

The authors declare no conflict of interest.

Data Availability Statement

The data that support the findings of this study are available from the corresponding author upon reasonable request.

Keywords

catalytic kinetics, high-value metals, lithium-oxygen batteries, recycling, spent lithium-ion batteries

Received: December 4, 2024
Revised: March 26, 2025
Published online:

[1] H. Ji, J. Wang, J. Ma, H.-M. Cheng, G. Zhou, *Chem. Soc. Rev.* **2023**, *52*, 8194.
[2] H. Yu, H. Yang, K. Chen, L. Yang, M. Huang, Z. Wang, H. Lv, C. Xu, L. Chen, X. Luo, *Energy Storage Mater.* **2024**, *67*, 103288.
[3] M. Jiao, Q. Zhang, C. Ye, Z. Liu, X. Zhong, J. Wang, C. Li, L. Dai, G. Zhou, H.-M. Cheng, *Proc. Natl. Acad. Sci. USA* **2022**, *119*, 2202202119.
[4] J.-H. Kang, J. Lee, J.-W. Jung, J. Park, T. Jang, H.-S. Kim, J.-S. Nam, H. Lim, K. R. Yoon, W.-H. Ryu, I.-D. Kim, H. R. Byon, *ACS Nano* **2020**, *14*, 14549.
[5] T. Liu, S. Zhao, Q. Xiong, J. Yu, J. Wang, G. Huang, M. Ni, X. Zhang, *Adv. Mater.* **2023**, *35*, 2208925.
[6] Z.-Z. Shen, Y.-Z. Zhang, C. Zhou, R. Wen, L.-J. Wan, *J. Am. Chem. Soc.* **2021**, *143*, 21604.
[7] F. Li, M.-L. Li, H.-F. Wang, X.-X. Wang, L.-J. Zheng, D.-H. Guan, L.-M. Chang, J.-J. Xu, Y. Wang, *Adv. Mater.* **2022**, *34*, 2107826.
[8] C. Zhao, Z. Yan, B. Zhou, Y. Pan, A. Hu, M. He, J. Liu, J. Long, *Angew. Chem., Int. Ed.* **2023**, *62*, 202302746.
[9] H. Yan, W.-W. Wang, T.-R. Wu, Y. Gu, K.-X. Li, D.-Y. Wu, M. Zheng, Q. Dong, J. Yan, B.-W. Mao, *J. Am. Chem. Soc.* **2023**, *145*, 11959.
[10] J. Wang, F. Pan, W. Chen, B. Li, D. Yang, P. Ming, X. Wei, C. Zhang, *Electrochem. Energy Rev.* **2023**, *6*, 6.
[11] H. Yu, G. Zhang, D. Zhang, R. Yang, X. Li, X. Zhang, G. Lian, H. Hou, Z. Guo, C. Hou, X. Yang, F. Dang, *Adv. Energy Mater.* **2024**, *14*, 2401509.
[12] C. Lim, A. R. Fairhurst, B. J. Ransom, D. Haering, V. R. Stamenkovic, *ACS Catal.* **2023**, *13*, 14874.
[13] F. Lin, M. Li, L. Zeng, M. Luo, S. Guo, *Chem. Rev.* **2023**, *123*, 12507.
[14] Y. Zhao, Q. Gu, K. Yin, L. Tao, Y. Li, H. Tan, Y. Yang, S. Guo, *Proc. Natl. Acad. Sci. USA* **2023**, *120*, 2301439120.
[15] L. Cao, L. Niu, T. Mueller, *Proc. Natl. Acad. Sci. USA* **2019**, *116*, 22044.
[16] Y. Yao, Q. Dong, A. Brozena, J. Luo, J. Miao, M. Chi, C. Wang, I. G. Kevrekidis, Z. J. Ren, J. Greeley, G. Wang, A. Anapolsky, L. Hu, *Science* **2022**, *376*, 151.
[17] W.-L. Hsu, C.-W. Tsai, A.-C. Yeh, J.-W. Yeh, *Nat. Rev. Chem.* **2024**, *8*, 471.
[18] Z. Zhong, Y. Tu, L. Zhang, J. Ke, C. Zhong, W. Tan, L. Wang, J. Zhang, H. Song, L. Du, Z. Cui, *ACS Catal.* **2024**, *14*, 2917.
[19] P. Zhang, X. Hui, Y. Nie, R. Wang, C. Wang, Z. Zhang, L. Yin, *Small* **2023**, *19*, 2206742.
[20] M. Zhang, Z. Chen, W. Shao, T. Tian, X. Wang, Z. Chen, W. Qiao, C. Gu, *J. Colloid Interface Sci.* **2023**, *652*, 69.
[21] W. Yan, X. Wang, M. Liu, K. Ma, L. Wang, Q. Liu, C. Wang, X. Jiang, H. Li, Y. Tang, G. Fu, *Adv. Funct. Mater.* **2023**, *34*, 2310487.
[22] L. Liu, J. Lu, Y. Yang, W. Ruettinger, X. Gao, M. Wang, H. Lou, Z. Wang, Y. Liu, X. Tao, L. Li, Y. Wang, H. Li, H. Zhou, C. Wang, Q. Luo, H. Wu, K. Zhang, J. Ma, X. Cao, L. Wang, F.-S. Xiao, *Science* **2024**, *383*, 94.
[23] Z. Wang, S. Chen, W. Wu, R. Chen, Y. Zhu, H. Jiang, L. Yu, N. Cheng, *Adv. Mater.* **2023**, *35*, 2301310.
[24] X. Hu, D. Zuo, S. Cheng, S. Chen, Y. Liu, W. Bao, S. Deng, S. J. Harris, J. Wan, *Chem. Soc. Rev.* **2023**, *52*, 1103.
[25] S. Liu, Y. Shen, Y. Zhang, B. Cui, S. Xi, J. Zhang, L. Xu, S. Zhu, Y. Chen, Y. Deng, W. Hu, *Adv. Mater.* **2021**, *34*, 2106973.
[26] Y. Yan, J. Lin, K. Huang, X. Zheng, L. Qiao, S. Liu, J. Cao, S. C. Jun, Y. Yamauchi, J. Qi, *J. Am. Chem. Soc.* **2023**, *145*, 24218.
[27] T. Yang, Y. L. Zhao, W. P. Li, C. Y. Yu, J. H. Luan, D. Y. Lin, L. Fan, Z. B. Jiao, W. H. Liu, X. J. Liu, J. J. Kai, J. C. Huang, C. T. Liu, *Science* **2020**, *369*, 427.
[28] T. Yang, B. X. Cao, T. L. Zhang, Y. L. Zhao, W. H. Liu, H. J. Kong, J. H. Luan, J. J. Kai, W. Kuo, C. T. Liu, *Mater. Today* **2022**, *52*, 161.
[29] C.-L. Yang, L.-N. Wang, P. Yin, J. Liu, M.-X. Chen, Q.-Q. Yan, Z.-S. Wang, S.-L. Xu, S.-L. Chu, S.-Q. Chu, C. Cui, H. Ju, H. Zhu, J. Zhu, Y. Lin, J. Shui, H.-W. Liang, *Science* **2021**, *374*, 459.
[30] S. Dai, Y. You, S. Zhang, W. Cai, M. Xu, L. Xie, R. Wu, G. W. Graham, *Nat. Commun.* **2017**, *8*, 204.
[31] J. Luo, J. Zhang, Z. Guo, Z. Liu, C. Wang, H. Jiang, J. Zhang, L. Fan, H. Zhu, Y. Xu, R. Liu, J. Ding, Y. Chen, W. Hu, *Adv. Mater.* **2024**, *36*, 2405956.
[32] H. Jin, Z. Xu, Z.-Y. Hu, Z. Yin, Z. Wang, Z. Deng, P. Wei, S. Feng, S. Dong, J. Liu, S. Luo, Z. Qiu, L. Zhou, L. Mai, B.-L. Su, D. Zhao, Y. Liu, *Nat. Commun.* **2023**, *14*, 1518.
[33] Z. Zhao, J. Sun, X. Li, S. Qin, C. Li, Z. Zhang, Z. Li, X. Meng, *Nat. Commun.* **2024**, *15*, 7475.

[34] F. Xiao, Y. Wang, G.-L. Xu, F. Yang, S. Zhu, C.-J. Sun, Y. Cui, Z. Xu, Q. Zhao, J. Jang, X. Qiu, E. Liu, W. S. Drisdell, Z. Wei, M. Gu, K. Amine, M. Shao, *J. Am. Chem. Soc.* **2022**, *144*, 20372.
[35] L. Zeng, Z. Zhao, F. Lv, Z. Xia, S.-Y. Lu, J. Li, K. Sun, K. Wang, Y. Sun, Q. Huang, Y. Chen, Q. Zhang, L. Gu, G. Lu, S. Guo, *Nat. Commun.* **2022**, *13*, 3822.
[36] Z. Zhang, Z. Zhang, C. Chen, R. Wang, M. Xie, S. Wan, R. Zhang, L. Cong, H. Lu, Y. Han, W. Xing, Z. Shi, S. Feng, *Nat. Commun.* **2024**, *15*, 2556.
[37] Y. Li, P. Kidkhunthod, Y. Zhou, X. Wang, J.-M. Lee, *Adv. Funct. Mater.* **2022**, *32*, 2205985.
[38] Y. Zhang, S. Zhang, J. Ma, X. Chen, C. Nan, C. Chen, *Angew. Chem., Int. Ed.* **2023**, *62*, 202218926.
[39] J.-J. Xu, Z.-W. Chang, Y. Wang, D.-P. Liu, Y. Zhang, X.-B. Zhang, *Adv. Mater.* **2016**, *28*, 9620.
[40] Y. Li, Y. Li, Y. Ding, J. Ma, P. Das, B. Zhang, Z.-S. Wu, X. Bao, *Chem Catal* **2023**, *3*, 100658.
[41] J. Qiu, Y. Lin, S. Zhang, J. Ma, Y. Zhang, M. Yuan, G. Sun, C. Nan, *Nano Res.* **2023**, *16*, 6798.
[42] G. Zhang, G. Li, J. Wang, H. Tong, J. Wang, Y. Du, S. Sun, F. Dang, *Adv. Energy Mater.* **2022**, *12*, 2103910.
[43] P. Wang, D. Zhao, P. Zhang, X. Hui, Z. Zhang, R. Wang, C. Wang, X. Ge, X. Liu, Y. C. Li, L. Yin, *Nat. Commun.* **2025**, *16*, 1453.
[44] J. Tian, Y. Rao, W. Shi, J. Yang, W. Ning, H. Li, Y. Yao, H. Zhou, S. Guo, *Angew. Chem., Int. Ed.* **2023**, *62*, 202310894.
[45] Z. Sun, X. Lin, C. Wang, Y. Tan, W. Dou, A. Hu, J. Cui, J. Fan, R. Yuan, M. Zheng, Q. Dong, *Adv. Mater.* **2024**, *36*, 2404319.
[46] Q. Lv, Z. Zhu, Y. Ni, B. Wen, Z. Jiang, H. Fang, F. Li, *J. Am. Chem. Soc.* **2022**, *144*, 23239.
[47] Z. Gou, Y. Yao, X. Geng, F. Yang, X. Hu, Z. Chen, L. Zheng, Y. Su, F. Wu, J. Lu, *Adv. Energy Mater.* **2024**, *14*, 2304272.
[48] C. Tan, D. Cao, L. Zheng, Y. Shen, L. Chen, Y. Chen, *J. Am. Chem. Soc.* **2022**, *144*, 807.
[49] M. Wang, J. Chen, Z. Tian, W. Dai, B. Cui, X. Cui, D. Wang, Y. Xiao, X. Lian, C. Jiang, H. Yang, Y. Wang, Z. Sun, Y. Ding, Y.-Y. Sun, J. Zhang, W. Chen, *Energy Environ. Sci.* **2023**, *16*, 523.
[50] P. Wang, Y. Ren, R. Wang, P. Zhang, M. Ding, C. Li, D. Zhao, Z. Qian, Z. Zhang, L. Zhang, L. Yin, *Nat. Commun.* **2020**, *11*, 1576.
[51] Y. Zhou, K. Yin, Q. Gu, L. Tao, Y. Li, H. Tan, J. Zhou, W. Zhang, H. Li, S. Guo, *Angew. Chem., Int. Ed.* **2021**, *60*, 26592.
[52] Q. Han, W. Guo, X. He, T. Liu, X. Liu, X. Zhu, T. Bian, L. Jiang, J. Lu, Y. Zhao, *Joule* **2022**, *6*, 381.
[53] P. Zhang, B. Han, X. Yang, Y. Zou, X. Lu, X. Liu, Y. Zhu, D. Wu, S. Shen, L. Li, Y. Zhao, J. S. Francisco, M. Gu, *J. Am. Chem. Soc.* **2022**, *144*, 2129.
[54] E. Zhang, A. Dong, K. Yin, C. Ye, Y. Zhou, C. Tan, M. Li, X. Zheng, Y. Wang, X. Gao, H. Li, D. Wang, S. Guo, *J. Am. Chem. Soc.* **2024**, *146*, 2339.
[55] Y. Guo, P. Wang, Y. Liu, S. Guo, L. Shi, J. Sun, Y. Tian, X. Wang, S. Zhao, Z. Liu, *Appl. Catal. B -Environ.* **2024**, *356*, 124203.
[56] L.-N. Song, W. Zhang, Y. Wang, X. Ge, L.-C. Zou, H.-F. Wang, X.-X. Wang, Q.-C. Liu, F. Li, J.-J. Xu, *Nat. Commun.* **2020**, *11*, 2191.
[57] J. Wei, H. Tang, L. Sheng, R. Wang, M. Fan, J. Wan, Y. Wu, Z. Zhang, S. Zhou, J. Zeng, *Nat. Commun.* **2024**, *15*, 559.
[58] Z. Sun, X. Lin, C. Wang, A. Hu, Q. Hou, Y. Tan, W. Dou, R. Yuan, M. Zheng, Q. Dong, *Angew. Chem., Int. Ed.* **2022**, *61*, 202207570.
[59] S. Ahn, C. Zor, S. Yang, M. Lagnoni, D. Dewar, T. Nimmo, C. Chau, M. Jenkins, A. J. Kibler, A. Pateman, G. J. Rees, X. Gao, P. Adamson, N. Grobert, A. Bertei, L. R. Johnson, P. G. Bruce, *Nat. Chem.* **2023**, *15*, 1022.
[60] Y. Cai, Y. Hou, Y. Lu, Q. Zhang, Z. Yan, J. Chen, *Angew. Chem., Int. Ed.* **2023**, *62*, 202218014.
[61] Y. Zhou, Q. Gu, Y. Xin, X. Tang, H. Wu, S. Guo, *Nano Lett.* **2023**, *23*, 10600.
[62] P. Wang, D. Zhao, X. Hui, Z. Qian, P. Zhang, Y. Ren, Y. Lin, Z. Zhang, L. Yin, *Adv. Energy Mater.* **2021**, *11*, 2003069.
[63] Y. Zhou, Q. Gu, K. Yin, Y. Li, L. Tao, H. Tan, Y. Yang, S. Guo, *Angew. Chem., Int. Ed.* **2022**, *61*, 202201416.
[64] J. Wang, Y. Zhang, S. Jiang, C. Sun, S. Song, *Angew. Chem., Int. Ed.* **2023**, *62*, 202307808.
[65] F. Xiao, Q. Bao, C. Sun, Y. Li, D. Cui, Q. Wang, F. Dang, H. Yu, G. Lian, *Adv. Energy Mater.* **2024**, *14*, 2303766.